TECHNISCHE MECHANIK
an open access journal

journal homepage: www.ovgu.de/techmech

Tech. Mech., Vol. 39, Is. 3, (2019), 261–281

Received: July 5, 2019
Accepted: September 18, 2019
Available online: October 1, 2019

Numerical Analysis of a Steam Turbine Rotor subjected to Thermo-Mechanical Cyclic Loads

J. Eisenträger[1]*, K. Naumenko[1], and H. Altenbach[1]

[1]Otto-von-Guericke-Universität, Institut für Mechanik, Universitätsplatz 2, 39106 Magdeburg, Germany

Abstract: The contribution at hand discusses the thermo-mechanical analysis of a steam turbine rotor, made of a heat-resistant steel. Thereby, the analysis accounts for the complicated geometry of a real steam turbine rotor, subjected to practical and complex thermo-mechanical boundary conditions. Various thermo-mechanical loading cycles are taken into account, including different starting procedures (cold and warm starts). Within the thermal analysis using the FE code ABAQUS, instationary steam temperatures as well as heat transfer coefficients are prescribed, and the resulting temperature field serves as input for the subsequent structural analysis. In order to describe the mechanical behavior of the heat-resistant steel, which exhibits significant rate-dependent inelasticity combined with hardening and softening phenomena, a robust nonlinear constitutive approach, the binary mixture model, is employed and implemented in ABAQUS in two different ways, i.e. using explicit as well as implicit methods for the time integration of the governing evolution equations. The numerical performance, the required computational effort, and the obtained accuracy of both integration methods are examined with reference to the thermo-mechanical analysis of a steam turbine rotor, as a typical practical example for the numerical analysis of a complex component. In addition, the obtained temperature, stress, and strain fields in the steam turbine rotor are discussed in detail, and the influence of the different starting procedures is examined closely.

Keywords: steam turbine rotor, mixture model, creep, numerical time integration, nonlinear constitutive modeling

1 Introduction

The current paper presents details on the thermo-mechanical analysis of a steam turbine rotor considering complex boundary conditions as well as the complicated geometry of this power plant component. In power plants, high temperatures prevail (around 873 K) such that the components operate under creep conditions, cf. Straub (1995); Fournier et al. (2011b); Pétry and Lindet (2009); Naumenko et al. (2011b); Götz (2004). Furthermore, the components are subjected to cyclic loads because of frequent start-ups and shut-downs of power plants, cf. Fournier et al. (2011a, 2005, 2009b, 2010); Röttger (1997). To withstand these conditions, heat-resistant steels with high chromium content offer excellent properties, e.g. high creep strength and good corrosion resistance, cf. Pétry and Lindet (2009); Götz (2004); Fournier et al. (2005); Berns and Theisen (2008); Giroux et al. (2010); Wang et al. (2013); Alsagabi et al. (2014); Kostenko et al. (2013), such that these alloys are commonly used for power plant components. Nevertheless, these steels tend to soften under creep-fatigue loads, which is based on microstructural processes such as the coarsening of subgrains and precipitates, cf. Straub (1995); Fournier et al. (2011b,a, 2009b, 2010); Röttger (1997); Giroux et al. (2010); Chilukuru et al. (2009); Agamennone et al. (2006); Orlová et al. (1998); Fournier et al. (2009a).

To the present, various constitutive models have been developed to simulate the mechanical behavior of high-chromium heat-resistant steels. Since a detailed survey of these approaches goes beyond the scope of this paper, we only provide a brief overview in the following. Overall, the constitutive models can be classified either as unified or non-unified approaches. The notion of unified model was introduced by Chaboche and Rousselier (1983). Thereby, only one time-dependent inelastic strain is taken into account. In contrast, non-unified models introduce separate variables to describe the instantaneous plastic strains and time-dependent inelastic deformation. Among the non-unified models, Wang et al. (2015) and Velay et al. (2006) present approaches for high-chromium heat-resistant steels. First, in Velay et al. (2006), the authors make use of internal variables to account for the cyclic behavior of a heat-resistant steel. In addition, Wang et al. (2015) adopt the Chaboche model, cf. Chaboche (1989), with three backstresses including both isotropic and kinematic hardening as well as a damage variable to simulate creep-fatigue behavior.

Moreover, the Chaboche model is frequently employed also in combination with unified constitutive models, cf. for example Saad (2012); Barrett et al. (2013); Zhang and Xuan (2017). All three chosen unified constitutive models are used to simulate the thermo-mechanical behavior of high-chromium heat-resistant steels, and 10 or even more temperature-dependent parameters are involved. Note that the actual number of parameters is at least twice as much since a minimum of two parameters is required to determine the (in the simplest case – linear) dependence on the temperature of each parameter. The large numbers of parameters frequently result from the introduction of several backstresses in order to account for nonlinear kinematic hardening. Consequently, the calibration effort increases and providing a physical background for all introduced parameters becomes a challenging task. For these reasons, we refrain from using the Chaboche model with several backstresses, and a unified mixture model is used to describe the thermo-mechanical behavior of the alloy X20CrMoV12-1, which is a typical heat-resistant steel with high chromium

* E-mail address: johanna.eisentraeger@ovgu.de
doi: 10.24352/UB.OVGU-2019-024

content.

Originally, the mixture model is based on materials science. Inelasticity combined with hardening and softening phenomena is simulated by applying an iso-strain concept to a binary mixture with a soft and hard constituent, cf. Straub (1995); Polcik (1998). The alloy under consideration is made of soft subgrains, which are separated by harder boundaries. Furthermore, the volume fraction of the hard constituent is closely related to the microstructure, for example the mean subgrain size. In order to model softening, we assume that the volume fraction of the hard constituent reduces during deformation until a saturation value is attained, cf. Naumenko et al. (2011a). Following the original formulation in materials science, the mixture models can be calibrated based on micrography, cf. e.g. Straub (1995); Polcik (1998); Barkar and Ågren (2005). However, if one would like to use results from macroscopic material tests for the calibration, the micromechanical mixture model must be transformed into a macroscopic approach. For this purpose, Naumenko et al. (2011a) introduce a backstress and a softening variable as internal variables. This macroscopic mixture model is calibrated in Eisenträger et al. (2018a) based on results from high temperature tensile tests and creep tests published in Eisenträger et al. (2017). After all, the mixture model describes the thermo-mechanical behavior of the considered heat-resistant steel over wide ranges of stresses and temperature ($100\,\mathrm{MPa} \leq \sigma \leq 700\,\mathrm{MPa}$, $673\,\mathrm{K} \leq T \leq 923\,\mathrm{K}$ with the Cauchy stress σ and the temperature T), while only 16 temperature-independent material parameters are involved, cf. Eisenträger (2018). To sum up, the mixture model features three main improvements in comparison to alternative approaches. Firstly, the number of material parameters is kept to a minimum since only two internal variables, i.e. a backstress and a softening variable, are taken into account. Secondly, it is possible to calibrate the model using only simple macroscopic tests, such that time-consuming microscopic observations are not necessary to identify all parameters. On top of that, one can apply the model to wide ranges of stresses and temperatures.

The current contribution aims at analyzing a steam turbine rotor with the calibrated mixture model. Note that the results of a similar analysis are presented in Eisenträger (2018). However, the analysis in Eisenträger (2018) focuses on a rotor with idealized geometry and simplified boundary conditions. To conduct this finite element analysis, the mixture model has been implemented into the FE code ABAQUS based on the implicit Euler method for time integration, cf. Eisenträger et al. (2018b). As a next step based on the previous publications, the contribution at hand demonstrates the applicability of the mixture model to a real power plant component with complicated geometry subjected to complex boundary conditions in step with actual practice. Note that several papers on finite element analysis of turbine rotors have already been published, cf. for example Jing et al. (2001, 2003); Nayebi et al. (2012); Sun et al. (2013); Wang et al. (2016); Zhu et al. (2017); Benaarbia et al. (2018); Wang and Liu (2018). Whereas the papers Nayebi et al. (2012); Benaarbia et al. (2018) refer to gas turbine rotors, the majority of publications focuses on steam turbine rotors. Furthermore, most authors make use of the Chaboche model to describe the multiaxial stress-strain behavior of the rotors. Axisymmetric FE models are frequently applied, and in many cases a preceding thermal analysis is conducted, which provides the temperature field as input for the subsequent structural analysis. Although these studies provide detailed insight into the stress and strain fields in rotors subjected to creep-fatigue loads, the influence of different starting procedures, such as varying initial temperatures in the rotor, has not been analyzed yet. Furthermore, in many cases, the given information on the applied boundary conditions could go more into detail. Consequently, the contribution at hand will address these problems by analyzing the influence of different starting procedures on the rotor as well as providing extensive and precise information on the applied boundary conditions. On top of that, we present a new implementation of the mixture model into the finite element method (FEM) based on explicit time integration of the evolution equations. This allows for a comparison of two different time integration methods (implicit and explicit Euler methods) with respect to their numerical performance, the involved computational effort, and the obtained accuracy. Although both time integration methods are well-known, most evaluations in literature focus on simple numerical examples, cf. Manzari and Prachathananukit (2001); Hu and Liu (2014). In contrast, the contribution at hand applies both methods to a complex problem taken from practice, whereby it is of particular interest to minimize computational times.

The current paper is composed of five sections, including this first introductory section. In Sect. 2, the governing equations of the binary mixture model are derived, and two internal variables, i.e. a backstress and a softening variable, are introduced. Section 3 focuses on the implementation of the mixture model into the FE code ABAQUS, based both on explicit and implicit time integration. The stress update algorithms as well as the consistent tangent operators are described for the two different time integration methods. Afterwards, details on the finite element analysis of the steam turbine rotor are given in Sect. 4. The section starts with a detailed description of the FE model, the meshes, as well as the boundary conditions. Subsequently, we examine the numerical performance of implicit and explicit time integration. We conclude the section by discussing the obtained temperature, stress, and strain fields in the rotor in detail. Finally, Sect. 5 gives a brief summary of the findings and identifies areas for further research.

Note that we make use both of direct tensor notation as well as matrix notation in this papers. While scalars are represented by italic letters, e.g. a, italic lowercase bold letters are used for vectors, e.g. $\boldsymbol{a} = a_i\,\boldsymbol{e}_i$. We symbolize tensors of second order by italic uppercase bold letters, e.g. $\boldsymbol{A} = A_{jk}\,\boldsymbol{e}_j \otimes \boldsymbol{e}_k$, and represent fourth-order tensors by upright uppercase double struck letters, for example $\mathbb{A} = A_{pqrs}\,\boldsymbol{e}_p \otimes \boldsymbol{e}_q \otimes \boldsymbol{e}_r \otimes \boldsymbol{e}_s$. Throughout the paper, Einstein's summation convention is applied, while Latin indices (e.g. i, j) take the values 1, 2, 3. Considering Cartesian coordinate systems with orthonormal bases, e.g. $\{\boldsymbol{e}_i\}$, we introduce the dyadic product:

$$\boldsymbol{a} \otimes \boldsymbol{b} = a_i\, b_j\, \boldsymbol{e}_i \otimes \boldsymbol{e}_j\,, \tag{1}$$

as well as the double scalar product between two tensors of second order and the analogous formulation for a fourth and a second-order tensor:

$$\boldsymbol{A} : \boldsymbol{B} = \left(A_{jk}\,\boldsymbol{e}_j \otimes \boldsymbol{e}_k\right) : \left(B_{no}\,\boldsymbol{e}_n \otimes \boldsymbol{e}_o\right) = A_{jk} B_{kj}\,, \tag{2}$$

$$\mathbb{A} : \boldsymbol{B} = \left(A_{jklm}\,\boldsymbol{e}_j \otimes \boldsymbol{e}_k \otimes \boldsymbol{e}_l \otimes \boldsymbol{e}_m\right) : \left(B_{no}\,\boldsymbol{e}_n \otimes \boldsymbol{e}_o\right) = A_{jklm} B_{ml} \boldsymbol{e}_j \otimes \boldsymbol{e}_k\,. \tag{3}$$

Here, it is worth noting that frequently, the double scalar product between two second-order tensors or a fourth and a second-order tensor is formulated in a different way in literature, cf. e.g. Itskov (2019). Switching to a vector-matrix notation, we represent vectors by upright lowercase sans serif bold letters, such as **a**. Matrices are symbolized by upright uppercase sans serif bold letters, e.g. **A**.

2 Constitutive Model

2.1 Binary Mixture Formulation

In the following, the governing equations of the binary mixture model are presented, based on the papers Naumenko et al. (2011a,b); Naumenko and Altenbach (2016); Eisenträger et al. (2018b). Since it is a *binary* mixture model, two constituents are taken into account: a "soft" and a "hard" part. While the soft constituent is related to regions with a low dislocation density, such as the interior of subgrains, the hard phase comprises the areas with a high dislocation density, i.e. the subgrain boundaries. Let us introduce the index $\square_k \forall\, k = \{\mathrm{s}, \mathrm{h}\}$ to distinguish the variables related to the different constituents.
Since the constitutive model will be utilized to simulate the thermo-mechanical behavior of practical components in power plants, the mixture model is formulated with respect to geometrically linear processes. Furthermore, due to this restriction, the involved computational effort decreases significantly. As already pointed out in Eisenträger et al. (2018b), in the case of applications involving high strains, various similar constitutive models for rate-dependent inelasticity under large deformations incorporating softening and hardening processes have been formulated, cf. Zhu et al. (2014); Shutov and Kreißig (2008). Because only geometrically linear processes are considered, we introduce the linear strain tensor $\boldsymbol{\varepsilon}$. The iso-strain assumption represents an important part of the mixture model, such that the strains in the two constituents are assumed to be equal:

$$\boldsymbol{\varepsilon} = \boldsymbol{\varepsilon}_\mathrm{h} = \boldsymbol{\varepsilon}_\mathrm{s}. \tag{4}$$

The iso-strain concept, which is also often referred to as "Voigt model" in literature, provides a robust and straightforward description of the material behavior. Nevertheless, one should point out that more sophisticated approaches are available as well in case if the constitutive model should be refined. For instance, one could use the continuum theory of mixtures, cf. Atkin and Craine (1976), to account for the interaction of the phases in the mixture. Furthermore, alternative models have been developed, which are neither founded upon the Voigt model nor the iso-stress (Reuss) concept. Instead, these approaches provide results that lie between the Voigt-Reuss bounds, for example the multiphase creep model presented in Raj et al. (1996).
The current constitutive model belongs to the group of unified material models, as introduced in Chaboche and Rousselier (1983). Here, the total inelastic strain $\boldsymbol{\varepsilon}_k^{\mathrm{in}}$ describes instantaneous plastic strains as well as creep strains, which are time-dependent. Note that the strains in both constituents are split additively into their elastic and inelastic portions, denoted by the superscripts $\square^{\mathrm{el}}$ and $\square^{\mathrm{in}}$, respectively:

$$\boldsymbol{\varepsilon} = \boldsymbol{\varepsilon}_k^{\mathrm{el}} + \boldsymbol{\varepsilon}_k^{\mathrm{in}}. \tag{5}$$

In addition, we make use of Hooke's law to describe the linear elastic behavior of isotropic materials:

$$\boldsymbol{\varepsilon}_k^{\mathrm{el}} = \frac{\sigma_{\mathrm{m}_k}}{3K}\boldsymbol{I} + \frac{\boldsymbol{\sigma}_k'}{2G} \tag{6}$$

or:

$$\boldsymbol{\sigma}_k = K\varepsilon_{\mathrm{V}_k}^{\mathrm{el}}\boldsymbol{I} + 2G\boldsymbol{\varepsilon}_k^{\mathrm{el}'}, \tag{7}$$

whereas the parameters G and K denote the shear and bulk modulus, respectively. Furthermore, we have introduced the Cauchy stress tensor $\boldsymbol{\sigma}$, the mean stress $\sigma_\mathrm{m} = \frac{1}{3}\mathrm{tr}\,(\boldsymbol{\sigma})$, and the volumetric strain $\varepsilon_\mathrm{V} = \mathrm{tr}\,(\boldsymbol{\varepsilon})$, which are computed based on the stress and strain tensors, applying the trace operator $\mathrm{tr}\,(\square)$. The deviatoric part of a second-order tensor is marked by the prime $\square' = \square - \frac{1}{3}\mathrm{tr}\,(\square)\,\boldsymbol{I}$, and the identity tensor of second order is represented by $\boldsymbol{I} = \boldsymbol{e}_i \otimes \boldsymbol{e}_i$. It is worth mentioning that the mixture model presumes an identical elastic behavior in both constituents, such that the same elastic material parameters are introduced for both constituents in Eqs. (6) and (7).
As a common choice to compute the total stress in a mixture model, a mixture rule based on the volume fractions η_k of the constituents is applied:

$$\boldsymbol{\sigma} = \eta_\mathrm{s}\boldsymbol{\sigma}_\mathrm{s} + \eta_\mathrm{h}\boldsymbol{\sigma}_\mathrm{h}, \tag{8}$$

while the following condition holds for the volume fractions due to conservation of mass:

$$\eta_\mathrm{s} + \eta_\mathrm{h} = 1 \qquad \forall \quad 0 \leq \eta_k \leq 1. \tag{9}$$

In order to simplify the constitutive model, let us only consider the volumetric parts of the stress and strain tensors in the following and apply the trace operator to Eqs. (4)–(6):

$$\varepsilon_\mathrm{V} = \varepsilon_{\mathrm{V}_\mathrm{h}} = \varepsilon_{\mathrm{V}_\mathrm{s}}, \tag{10}$$

$$\varepsilon_\mathrm{V} = \varepsilon_{\mathrm{V}_k}^{\mathrm{el}} + \varepsilon_{\mathrm{V}_k}^{\mathrm{in}}, \tag{11}$$

$$\varepsilon_{\mathrm{V}_k}^{\mathrm{el}} = \frac{\sigma_{\mathrm{m}_k}}{K}. \tag{12}$$

Within the classical theory of plastic deformations, it is commonly accepted to assume that the inelastic strains are not affected by the spherical part of the stresses, i.e. $\varepsilon_{\mathrm{V}_k}^{\mathrm{in}} = 0 \Rightarrow \boldsymbol{\varepsilon}_k^{\mathrm{in}} = \boldsymbol{\varepsilon}_k^{\mathrm{in}'}$. Considering this assumption and inserting Eqs. (11) and (12) into Eq. (10) yield:

$$\sigma_{\mathrm{m}} = \sigma_{\mathrm{m_h}} = \sigma_{\mathrm{m_s}} = K\varepsilon_{\mathrm{V}}. \tag{13}$$

Due to the equal bulk moduli in both constituents, Eq. (13) reveals that the mean stresses are equal in the entire mixture. Thus, one can restrict Eqs. (4) and (8) to the deviatoric parts of the stress and strain tensors:

$$\boldsymbol{\varepsilon}' = \boldsymbol{\varepsilon}_{\mathrm{h}}' = \boldsymbol{\varepsilon}_{\mathrm{s}}', \tag{14}$$

$$\boldsymbol{\sigma}' = \eta_{\mathrm{s}}\boldsymbol{\sigma}_{\mathrm{s}}' + \eta_{\mathrm{h}}\boldsymbol{\sigma}_{\mathrm{h}}'. \tag{15}$$

Next, we determine the stress deviators $\boldsymbol{\sigma}_k'$ for both constituents based on Eq. (6). The obtained expressions for the deviatoric stresses are inserted into Eq. (15), which yields the constitutive law for the elastic behavior of the entire mixture:

$$\boldsymbol{\varepsilon} = \frac{\sigma_{\mathrm{m}}}{3K}\boldsymbol{I} + \frac{\boldsymbol{\sigma}'}{2G} + \boldsymbol{\varepsilon}^{\mathrm{in}}, \tag{16}$$

while $\boldsymbol{\varepsilon}^{\mathrm{in}}$ represents the inelastic strain of the mixture:

$$\boldsymbol{\varepsilon}^{\mathrm{in}} \equiv (1-\eta_{\mathrm{h}})\,\boldsymbol{\varepsilon}_{\mathrm{s}}^{\mathrm{in}} + \eta_{\mathrm{h}}\boldsymbol{\varepsilon}_{\mathrm{h}}^{\mathrm{in}}. \tag{17}$$

In addition, evolution equations for the inelastic strains $\dot{\boldsymbol{\varepsilon}}_k^{\mathrm{in}}$ are formulated, following Naumenko et al. (2011a); Naumenko and Altenbach (2016):

$$\dot{\boldsymbol{\varepsilon}}_{\mathrm{s}}^{\mathrm{in}} = \frac{3}{2}\dot{\varepsilon}_{\mathrm{vM_s}}^{\mathrm{in}}\frac{\boldsymbol{\sigma}_{\mathrm{s}}'}{\sigma_{\mathrm{vM_s}}}, \tag{18}$$

$$\dot{\boldsymbol{\varepsilon}}_{\mathrm{h}}^{\mathrm{in}} = \frac{3}{2}\dot{\varepsilon}_{\mathrm{vM}}^{\mathrm{in}}\frac{\boldsymbol{\sigma}_{\mathrm{h}}' - \boldsymbol{\sigma}'}{\sigma_{\mathrm{vM}_\star}}. \tag{19}$$

Note that we have introduced the von Mises equivalent inelastic strain rates $\dot{\varepsilon}_{\mathrm{vM_s}}^{\mathrm{in}}$ and $\dot{\varepsilon}_{\mathrm{vM}}^{\mathrm{in}}$ for the soft part and with respect to the entire mixture, respectively. Furthermore, the variable $\sigma_{\mathrm{vM_s}}$ denotes the von Mises equivalent stress in the soft constituent, and $\sigma_{\mathrm{vM}_\star}$ is the von Mises equivalent saturation stress:

$$\dot{\varepsilon}_{\mathrm{vM_s}}^{\mathrm{in}} = \sqrt{\frac{2}{3}\dot{\boldsymbol{\varepsilon}}_{\mathrm{s}}^{\mathrm{in}} : \dot{\boldsymbol{\varepsilon}}_{\mathrm{s}}^{\mathrm{in}}}, \tag{20}$$

$$\dot{\varepsilon}_{\mathrm{vM}}^{\mathrm{in}} = \sqrt{\frac{2}{3}\dot{\boldsymbol{\varepsilon}}^{\mathrm{in}} : \dot{\boldsymbol{\varepsilon}}^{\mathrm{in}}}, \tag{21}$$

$$\sigma_{\mathrm{vM_s}} = \sqrt{\frac{3}{2}\boldsymbol{\sigma}_{\mathrm{s}}' : \boldsymbol{\sigma}_{\mathrm{s}}'}, \tag{22}$$

$$\sigma_{\mathrm{vM}_\star} = \sqrt{\frac{3}{2}\left(\boldsymbol{\sigma}_{\mathrm{h}_\star}' - \boldsymbol{\sigma}'\right) : \left(\boldsymbol{\sigma}_{\mathrm{h}_\star}' - \boldsymbol{\sigma}'\right)}. \tag{23}$$

In above expressions, the term $\boldsymbol{\sigma}_{\mathrm{h}_\star}'$ stands for the saturation stress in the hard constituent. Additionally, the subsequent evolution equation is utilized for the equivalent inelastic strain rate in the soft constituent $\dot{\varepsilon}_{\mathrm{vM_s}}^{\mathrm{in}}$:

$$\dot{\varepsilon}_{\mathrm{vM_s}}^{\mathrm{in}} = f_\sigma\left(\sigma_{\mathrm{vM_s}}\right) f_T\left(T\right). \tag{24}$$

Moreover, we formulate an evolution equation for the volume fraction of the hard constituent:

$$\dot{\eta}_{\mathrm{h}} = f_\eta\left(\boldsymbol{\sigma}_{\mathrm{h}}, \dot{\boldsymbol{\varepsilon}}_{\mathrm{h}}^{\mathrm{in}}, T\right). \tag{25}$$

Note that the volume fraction of the soft constituent can be computed by combining Eqs. (9) and (25). The one-dimensional mixture model is visualized with rheological elements in Fig. 1, while we presume constant volume fractions in both constituents.

2.2 Formulation with Internal Variables

Since the mixture model has been described in the previous section in close reference to the microstructure, detailed microstructural observations would be required for the calibration of the model. Though, for the discussed application and the considered heat-resistant steel, we frequently only have access to the results of macroscopic material tests, such as high temperature tensile tests or creep tests. Therefore, we introduce two internal variables, i.e. a backstress tensor $\boldsymbol{\beta}$ and a dimensionless scalar softening

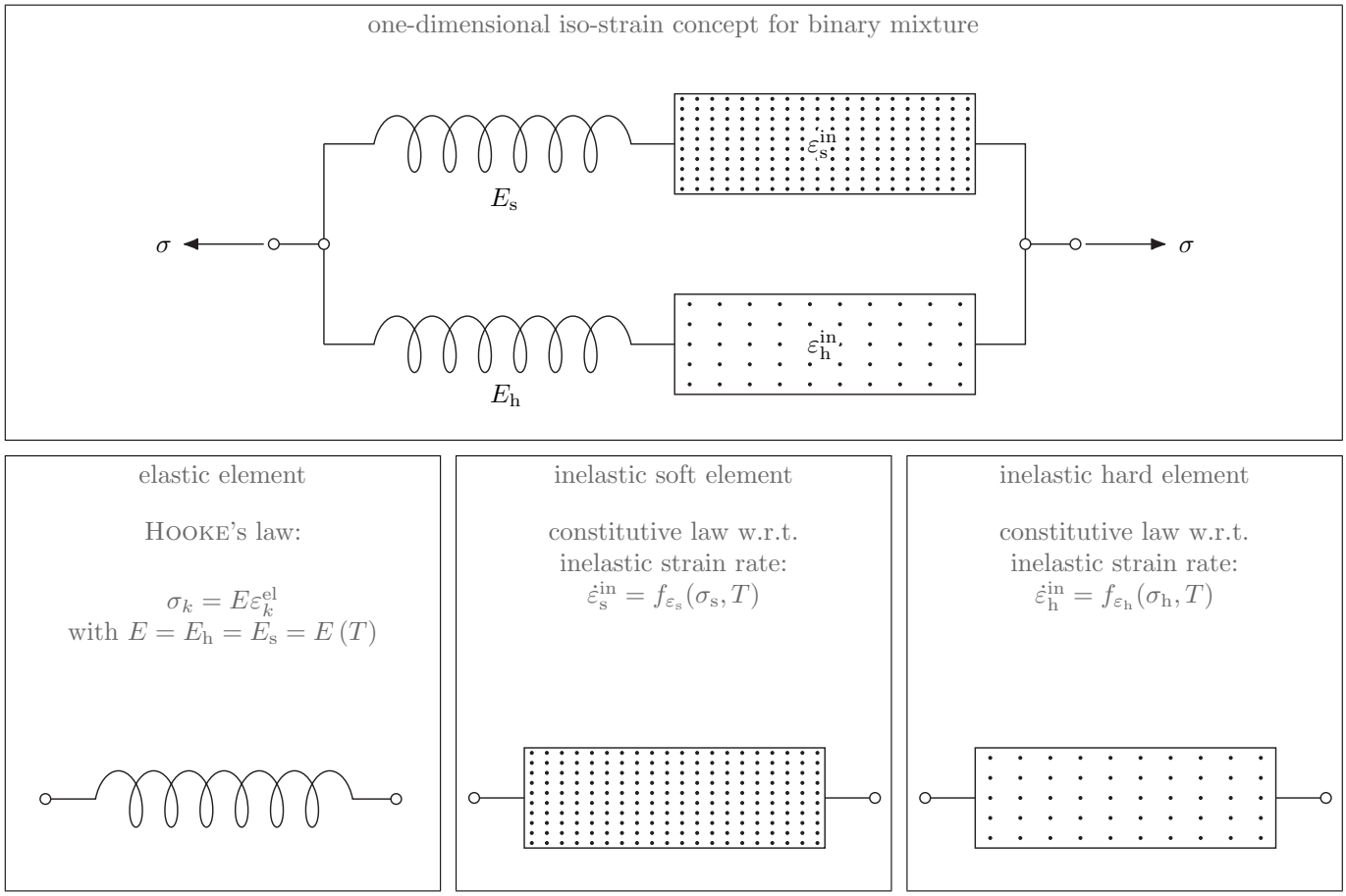

Fig. 1: Iso-strain concept for a binary mixture with constant volume fractions of constituents, cf. Eisenträger et al. (2017)

variable Γ. The backstress is employed to describe kinematic hardening. The tensorial variable as well as the corresponding equivalent von Mises variable β_vM are computed according to the following equations:

$$\boldsymbol{\beta} = \frac{\eta_{\mathrm{h}_0}}{1-\eta_{\mathrm{h}_0}}\left(\boldsymbol{\sigma}'_\mathrm{h} - \boldsymbol{\sigma}'\right) \qquad \forall \quad 0 < \eta_{\mathrm{h}_0} < 1, \tag{26}$$

$$\beta_\mathrm{vM} = \sqrt{\frac{3}{2}\boldsymbol{\beta}:\boldsymbol{\beta}} \qquad \forall \quad 0 \leq \beta_\mathrm{vM} \leq \beta_{\mathrm{vM}_\star}, \tag{27}$$

whereas the corresponding saturation values are marked with an asterisk:

$$\boldsymbol{\beta}_\star = \frac{\eta_{\mathrm{h}_0}}{1-\eta_{\mathrm{h}_0}}\left(\boldsymbol{\sigma}'_{\mathrm{h}_\star} - \boldsymbol{\sigma}'\right), \tag{28}$$

$$\beta_{\mathrm{vM}_\star} = \sqrt{\frac{3}{2}\boldsymbol{\beta}_\star:\boldsymbol{\beta}_\star}. \tag{29}$$

In Eqs. (26) and (28), we make use of the parameter η_{h_0}, denoting the volume fraction of the hard constituent in the initial state: $\eta_{\mathrm{h}_0} = \eta_\mathrm{h}\,(t=0)$. Moreover, it is demonstrated in Naumenko et al. (2011a) that the tensor $\boldsymbol{\beta}$ can be interpreted as a backstress similar to the well-known Armstrong-Frederick-type backstress, cf. Armstrong and Frederick (1966). To describe softening processes, the scalar variable Γ with the corresponding saturation value $\Gamma_\star$ is introduced in the following:

$$\Gamma = \frac{\eta_\mathrm{h}}{1-\eta_\mathrm{h}}\frac{1-\eta_{\mathrm{h}_0}}{\eta_{\mathrm{h}_0}} \qquad \forall \quad \Gamma_\star \leq \Gamma \leq 1, \tag{30}$$

$$\Gamma_\star = \frac{\eta_{\mathrm{h}\star}}{1-\eta_{\mathrm{h}\star}}\frac{1-\eta_{\mathrm{h}_0}}{\eta_{\mathrm{h}_0}} \qquad \forall \quad 0 < \eta_{\mathrm{h}\star} < 1. \tag{31}$$

Note that the new variable $\eta_{\mathrm{h}\star}$ represents the saturation value for the volume fraction with respect to the hard constituent. In the next step, we compute the stresses and inelastic strain rates of the individual constituents based on the new internal variables by deploying the definitions in Eqs. (26)–(31) as well as the Eqs. (15), (18), (19), and (24):

$$\boldsymbol{\sigma}'_\mathrm{h} = \boldsymbol{\sigma}' + \frac{1-\eta_{\mathrm{h}_0}}{\eta_{\mathrm{h}_0}}\boldsymbol{\beta}, \tag{32}$$

$$\boldsymbol{\sigma}'_\mathrm{s} = \tilde{\boldsymbol{\sigma}}', \tag{33}$$

$$\dot{\boldsymbol{\varepsilon}}_{\mathrm{h}}^{\mathrm{in}} = \frac{3}{2}\dot{\varepsilon}_{\mathrm{vM}}^{\mathrm{in}}\frac{\boldsymbol{\beta}}{\beta_{\mathrm{vM}_\star}}, \tag{34}$$

$$\dot{\boldsymbol{\varepsilon}}_{\mathrm{s}}^{\mathrm{in}} = \frac{3}{2}f_\sigma\left(\tilde{\sigma}_{\mathrm{vM}}\right)f_T\left(T\right)\frac{\tilde{\boldsymbol{\sigma}}'}{\tilde{\sigma}_{\mathrm{vM}}}, \tag{35}$$

while the effective stress $\tilde{\boldsymbol{\sigma}}'$ and the corresponding von Mises variable $\tilde{\sigma}_{\mathrm{vM}}$ have been introduced:

$$\tilde{\boldsymbol{\sigma}}' = \boldsymbol{\sigma}' - \Gamma\boldsymbol{\beta}, \tag{36}$$

$$\tilde{\sigma}_{\mathrm{vM}} = \sqrt{\frac{3}{2}\tilde{\boldsymbol{\sigma}}' : \tilde{\boldsymbol{\sigma}}'}. \tag{37}$$

Afterwards, Eq. (16) is differentiated with respect to the time t:

$$\dot{\boldsymbol{\varepsilon}}^{\mathrm{in}} = \dot{\boldsymbol{\varepsilon}} - \frac{\partial}{\partial t}\left(\frac{\sigma_{\mathrm{m}}}{3K}\boldsymbol{I} + \frac{\boldsymbol{\sigma}'}{2G}\right). \tag{38}$$

By taking into account Eq. (6), we transform Eq. (5) with respect to the individual constituents in a similar way:

$$\dot{\boldsymbol{\varepsilon}} = \frac{\partial}{\partial t}\left(\frac{\sigma_{\mathrm{m}}}{3K}\boldsymbol{I} + \frac{\boldsymbol{\sigma}_k'}{2G}\right) + \dot{\boldsymbol{\varepsilon}}_k^{\mathrm{in}}. \tag{39}$$

Finally, above equation is referred to the soft constituent and inserted into Eq. (38). In addition, one replaces the stress deviator $\boldsymbol{\sigma}_{\mathrm{s}}'$ and the inelastic strain rate tensor $\dot{\boldsymbol{\varepsilon}}_{\mathrm{s}}^{\mathrm{in}}$ by deploying Eqs. (33) and (35). Then, the equations are transformed until we obtain an evolution equation for the inelastic strain $\boldsymbol{\varepsilon}^{\mathrm{in}}$ in the mixture:

$$\dot{\boldsymbol{\varepsilon}}^{\mathrm{in}} = \frac{3}{2}f_\sigma\left(\tilde{\sigma}_{\mathrm{vM}}\right)f_T\left(T\right)\frac{\tilde{\boldsymbol{\sigma}}'}{\tilde{\sigma}_{\mathrm{vM}}} - \frac{\partial}{\partial t}\left(\frac{\Gamma\boldsymbol{\beta}}{2G}\right). \tag{40}$$

Note that the last term exerts only a slight influence on the inelastic strain rate at the beginning of inelastic deformation such that it is neglected in the remainder, as also already done in Naumenko et al. (2011a); Eisenträger et al. (2017). Thus, Eq. (40) is simplified as follows:

$$\dot{\boldsymbol{\varepsilon}}^{\mathrm{in}} = \frac{3}{2}f_\sigma\left(\tilde{\sigma}_{\mathrm{vM}}\right)f_T\left(T\right)\frac{\tilde{\boldsymbol{\sigma}}'}{\tilde{\sigma}_{\mathrm{vM}}}. \tag{41}$$

Finally, the equations for the hard constituent are transformed in an analogous way: First, we evaluate Eq. (39) with respect to the hard constituent and insert the resulting terms into Eq. (38). Thereby, the deviatoric stress $\boldsymbol{\sigma}_{\mathrm{h}}'$ and the inelastic strain rate $\dot{\boldsymbol{\varepsilon}}_{\mathrm{h}}^{\mathrm{in}}$ are substituted using Eqs. (32) and (34), which results in an evolution equation for the backstress $\boldsymbol{\beta}$:

$$\dot{\boldsymbol{\beta}} = \frac{1}{G}\frac{\partial G}{\partial T}\dot{T}\boldsymbol{\beta} + 2G\frac{\eta_{\mathrm{h}_0}}{1-\eta_{\mathrm{h}_0}}\left(\dot{\boldsymbol{\varepsilon}}^{\mathrm{in}} - \frac{3}{2}\dot{\varepsilon}_{\mathrm{vM}}^{\mathrm{in}}\frac{\boldsymbol{\beta}}{\beta_{\mathrm{vM}_\star}}\right). \tag{42}$$

Furthermore, we adopt the evolution equation for the softening variable from Naumenko et al. (2011a):

$$\dot{\Gamma} = C\left[\Gamma_\star\left(\sigma_{\mathrm{vM}}\right) - \Gamma\right]\dot{\varepsilon}_{\mathrm{vM}}^{\mathrm{in}}. \tag{43}$$

Since the volume fraction of the hard constituent is replaced by Γ, see also Eq. (30), Eq. (43) expresses the continuous decline of the softening variable towards its saturation value $\Gamma_\star$ as the inelastic deformation increases. In this way, we can describe the macroscopic softening of heat-resistant steels, which is based predominantly on the growth of subgrains. Note that this evolution equation is restricted to proportional loading, and in case of non-proportional loading, one should resort to refined approaches, as the model proposed in Silbermann et al. (2014).

The presented mixture model has been calibrated in Eisenträger et al. (2018a); Eisenträger (2018) based on the results of macroscopic material tests on the heat-resistant steel X20CrMoV12-1, as presented in Eisenträger et al. (2017). The following stress and temperature response functions have been found to describe the mechanical behavior of the heat-resistant alloy in a robust way:

$$E\left(T\right) = C_1 + C_2T^3, \tag{44}$$

$$G\left(T\right) = C_3 + C_4T^3, \tag{45}$$

$$f_T\left(T\right) = \exp\left(-\frac{Q}{\mathrm{R}T}\right), \tag{46}$$

$$f_\sigma\left(\tilde{\sigma}_{\mathrm{vM}}\right) = a_\sigma\sinh\left(\frac{\tilde{\sigma}_{\mathrm{vM}}}{b_\sigma}\right)\left[1 + \left(\frac{\tilde{\sigma}_{\mathrm{vM}}}{c_\sigma}\right)^{m_\sigma}\right], \tag{47}$$

$$\beta_{\mathrm{vM}_\star}\left(\sigma_{\mathrm{vM}}\right) = \frac{2a_\beta}{1+\exp\left(-b_\beta\sigma_{\mathrm{vM}}\right)} - a_\beta, \tag{48}$$

Tab. 1: Used constants and identified material parameters in the unified mixture model, cf. Eisenträger (2018)

variable	value	unit	meaning	equation
C_1	2.23×10^5	MPa	parameters in the temperature response function for YOUNG's modulus	(44)
C_2	-1.64×10^{-4}	MPa K^{-3}		
C_3	82.6×10^3	MPa	parameters in the temperature response function for shear modulus	(45)
C_4	-2.87×10^{-5}	MPa K^{-3}		
Q	540.6×10^3	J mol^{-1}	activation energy in the temperature response functions for the inelastic strain rate	(46)
R	8.317	J (mol K)$^{-1}$	universal gas constant in the temperature response functions for the inelastic strain rate	(46)
a_σ	1.54×10^{24}	s^{-1}	parameters in the stress response function for the inelastic strain rate	(47)
b_σ	25.8	MPa		
c_σ	483.6	MPa		
m_σ	35.7	–		
η_{h_0}	0.17	–	reference value for the volume fraction of the hard constituent	(42)
a_β	80.0	MPa	maximum value for the saturation backstress	(48)
b_β	2.70×10^{-2}	MPa^{-1}	parameter in the evolution function for the saturation backstress	(48)
C	5.0	–	parameter in the evolution equation for the softening variable	(43)
a_Γ	1.0	–	parameters in the stress response function for the saturation softening variable	(49)
b_Γ	1.30×10^{-2}	MPa^{-1}		
c_Γ	520.0	MPa		

$$\Gamma_\star\left(\sigma_{\mathrm{vM}}\right) = \frac{a_\Gamma}{1 + \exp\left[-b_\Gamma\left(\sigma_{\mathrm{vM}} - c_\Gamma\right)\right]}. \tag{49}$$

Note that a temperature response function for the YOUNG's modulus has been formulated since this material parameter is straightforward to determine based on high temperature tensile tests. The bulk modulus K is obtained based on the YOUNG's and shear modulus as follows:

$$K = \frac{GE}{3\left(3G - E\right)}. \tag{50}$$

Table 1 provides an overview of all constants and identified parameters. After all, the mixture model involves a total of 16 temperature-independent parameters, which is a relatively low number if we consider the remarkably wide ranges of applicability with respect to temperatures ($673\,\mathrm{K} \leq T \leq 923\,\mathrm{K}$) and stresses ($100\,\mathrm{MPa} \leq \sigma_{\mathrm{vM}} \leq 700\,\mathrm{MPa}$), as discussed in Eisenträger (2018). To provide a basis for the derivations in the following sections, let us recall the governing equations of the mixture model:

- HOOKE's law for the linear elastic behavior of the mixture, assuming isotropy

$$\boldsymbol{\sigma} = K\varepsilon_{\mathrm{V}}^{\mathrm{el}}\boldsymbol{I} + 2G\boldsymbol{\varepsilon}^{\mathrm{el}'}, \tag{51}$$

- the split of strains into the elastic and inelastic parts

$$\boldsymbol{\varepsilon} = \boldsymbol{\varepsilon}^{\mathrm{el}} + \boldsymbol{\varepsilon}^{\mathrm{in}}, \tag{52}$$

- the evolution equation for the inelastic strain, cf. Eq. (41),
- the evolution equation for the backstress, cf. Eq. (42),
- the evolution equation for the softening variable, cf. Eq. (43).

In addition, initial conditions (ICs) must be taken into account. In order to simulate the behavior of an undeformed material, we assume the following ICs:

$$\boldsymbol{\sigma}\left(t=0\right) = \mathbf{0}, \qquad \boldsymbol{\beta}\left(t=0\right) = \mathbf{0}, \qquad \Gamma\left(t=0\right) = 1. \tag{53}$$

Since the presented mixture model will be used in partly coupled thermo-mechanical analyses, it is of particular importance to check for thermodynamical consistency. In Eisenträger (2018), a proof for the thermodynamical consistency of the mixture model in the present form is given based on the CLAUSIUS-PLANCK inequality. Note that the proof of thermodynamical consistency is based on the assumption of stationary temperatures, which is deemed adequate considering the major applications, i.e. during the start-ups and shut-downs of power plants, temperatures change relatively slowly. The interested reader is referred to Eisenträger (2018), where further details on the derivation can be found.

3 Numerical Implementation

The analysis of a real steam turbine rotor featuring complex geometry and boundary conditions represents the overall aim of this contribution. Due to the complexity of the problem, the finite element method (FEM) is utilized as an established and versatile computational approach. Therefore, the current section provides details on the integration of the calibrated mixture model into the FEM.

In the previous section, it has been shown that the mixture model results in a system of five governing equations, i.e. Eqs. (51) and (52) as well as three evolution equations with respect to the inelastic strain $\boldsymbol{\varepsilon}^{\mathrm{in}}$, the backstress $\boldsymbol{\beta}$, and the softening variable Γ, cf. Eqs. (41)–(43). Note that displacement increments are usually prescribed in finite element calculations. The strains are straightforward to compute using the first derivatives of the displacement, while the stresses and internal variables are obtained based on the constitutive model — a process which is frequently referred to as stress update algorithm, cf. Belytschko et al. (2000). For this purpose, an evolution equation for the stress tensor $\boldsymbol{\sigma}$ is derived in the following by differentiating Eq. (16) with respect to time:

$$\dot{\boldsymbol{\sigma}} = K\dot{\varepsilon}_{\mathrm{V}}\boldsymbol{I} + 2G\left(\dot{\boldsymbol{\varepsilon}} - \dot{\boldsymbol{\varepsilon}}^{\mathrm{in}}\right) + \left(\frac{\partial K}{\partial T} + \frac{2}{3}\frac{\partial G}{\partial T}\right)\dot{T}\frac{\sigma_{\mathrm{m}}}{K}\boldsymbol{I} + \frac{1}{G}\frac{\partial G}{\partial T}\dot{T}\boldsymbol{\sigma}', \tag{54}$$

whereby the inelastic strain rate $\dot{\boldsymbol{\varepsilon}}^{\mathrm{in}}$ is computed by Eq. (41), involving the two internal variables. Next, we have to integrate the obtained system of evolution equations, i.e. Eqs. (42), (43), and (54), with respect to time, while displacement or strain increments are prescribed. To realize the time integration numerically, we can resort to two general classes of computational models for time integration: explicit and implicit approaches. In order to predict an unknown equilibrium state with respect to the time step t_{n+1}, explicit methods only require quantities from the previous time step t_n, cf. Wriggers (2008), which simplifies the implementation of explicit methods significantly. However, this type of time integration method exhibits only conditional stability, such that the stability is dependent on the selected time step size, cf. Luccioni et al. (2001).

Alternatively, implicit time integration methods can be used. Here, the variables for the new equilibrium state at the time step t_{n+1} are estimated by using not only the previous time steps, but taking into account the current and future time steps as well. This procedure usually results in the solution of a nonlinear system of equations at every time step, cf. Wriggers (2008), which increases the involved computational effort. Furthermore, the application of implicit time integration methods to nonlinear material models can be cumbersome. However, implicit methods feature unconditional stability, i.e. the stability is independent from the increment size, which represents a major advantage in comparison to explicit methods.

Since the previous considerations clearly show that both explicit and implicit methods feature different benefits and drawbacks, the contribution at hand discusses the implementation of the mixture model into the FEM based on both types of time integration methods. Note that Sect. 4.2 provides a detailed discussion of the accuracy and computational costs of both integration methods with respect to the finite element analysis of the steam turbine rotor. As a well-known approach both for implicit and explicit methods, we will make use of the backward and forward Euler methods for the numerical integration of the evolution equations. Due to their straightforward formulation, these methods are frequently employed to implement nonlinear constitutive models, cf. Hartmann and Haupt (1993); Hartmann et al. (1997); Kobayashi et al. (2003); Benaarbia et al. (2018).

In order to illustrate the general difference in explicit and implicit time integration, suppose that we would like to find a solution for the ordinary differential equation $\dot{\boldsymbol{Z}} = \boldsymbol{F}(\boldsymbol{Z}, t)$ with respect to the unknown variable $\boldsymbol{Z}$. The time increment Δt is prescribed, and the variable $\boldsymbol{Z}_n$ at the time step t_n is known. As a typical implicit time integration approach, the backward Euler method provides the solution at the time step $t_{n+1} = t_n + \Delta t$ as follows, cf. Simo and Hughes (1998); Belytschko et al. (2000); Zienkiewicz and Taylor (2005); Wriggers (2008):

$$\boldsymbol{Z}_{n+1} = \boldsymbol{Z}_n + \Delta t\, \boldsymbol{F}(\boldsymbol{Z}_{n+1}, t_{n+1})\,. \tag{55}$$

In contrast, if we apply the forward Euler method as an explicit method to the same problem, the solution requires only variables from the previous time step t_n, cf. Simo and Hughes (1998); Belytschko et al. (2000); Zienkiewicz and Taylor (2005); Wriggers (2008):

$$\boldsymbol{Z}_{n+1} = \boldsymbol{Z}_n + \Delta t\, \boldsymbol{F}(\boldsymbol{Z}_n, t_n)\,. \tag{56}$$

In the following, both methods are applied to the mixture model. The implicit time integration, including the stress update algorithm and the consistent tangent operator, is presented in Sect. 3.1, while Sect. 3.2 focuses on the explicit time integration. Whereas the derivations in Sect. 3.1 are based on Eisenträger et al. (2018b), the implementation of the mixture model using an explicit integration method has not been presented in literature yet.

3.1 Implicit Time Integration

3.1.1 Stress Update Algorithm

To update the stresses and internal variables based on the implicit Euler method, let us apply Eq. (55) to the governing equations of the mixture model. Using the backward Euler method, the strains, the temperature, the stress, and the internal variables are updated as follows, cf. Belytschko et al. (2000):

$$\square_{n+1} = \square_n + \Delta\, \square_{n+1} \qquad \forall \quad \square = \left\{\boldsymbol{\varepsilon}, \boldsymbol{\varepsilon}^{\mathrm{in}}, T, \boldsymbol{\sigma}, \boldsymbol{\beta}, \Gamma\right\}. \tag{57}$$

Note that in the remainder of this section all entities refer to the time step t_{n+1}, if it is not stated otherwise. Additionally, the evolution equations, cf. Eqs. (41)–(43), are transformed based on the backward Euler method:

$$\Delta\boldsymbol{\varepsilon}^{\mathrm{in}}_{n+1} = \frac{3}{2}\Delta t\, f_\sigma\left(\tilde{\sigma}_{\mathrm{vM}}\right) f_T\left(T\right) \frac{\tilde{\boldsymbol{\sigma}}'}{\tilde{\sigma}_{\mathrm{vM}}}, \tag{58}$$

$$\Delta\boldsymbol{\beta}_{n+1} = \frac{1}{G}\frac{\mathrm{d}G}{\mathrm{d}T}\Delta T\boldsymbol{\beta} + 2G\frac{\eta_{\mathrm{h}_0}}{1-\eta_{\mathrm{h}_0}}\left(\Delta\boldsymbol{\varepsilon}^{\mathrm{in}} - \frac{3}{2}\Delta\varepsilon^{\mathrm{in}}_{\mathrm{vM}}\frac{\boldsymbol{\beta}}{\beta_{\mathrm{vM}_\star}}\right), \tag{59}$$

$$\Delta\Gamma_{n+1} = C_\Gamma\left[\Gamma_\star\left(\sigma_{\mathrm{vM}}\right) - \Gamma\right]\Delta\varepsilon^{\mathrm{in}}_{\mathrm{vM}}. \tag{60}$$

Furthermore, we deploy Hooke's law by reformulating Eq. (51):

$$\boldsymbol{\sigma}_{n+1} = \mathbb{C}_{n+1} : \boldsymbol{\varepsilon}^{\mathrm{el}}_{n+1}, \tag{61}$$

whereby the elastic stiffness tensor $\mathbb{C}$ and the fourth-order identity tensor $\mathbb{I}$ are introduced:

$$\mathbb{C} = \frac{1}{3}\left(3K - 2G\right)\boldsymbol{I}\otimes\boldsymbol{I} + 2G\mathbb{I}, \tag{62}$$

$$\mathbb{I} = \frac{1}{2}\left(\boldsymbol{e}_i\otimes\boldsymbol{e}_j\otimes\boldsymbol{e}_j\otimes\boldsymbol{e}_i + \boldsymbol{e}_i\otimes\boldsymbol{e}_j\otimes\boldsymbol{e}_i\otimes\boldsymbol{e}_j\right). \tag{63}$$

Next, we substitute the elastic strain in Eq. (61) by making use of the additive split of strains, cf. Eq. (52), under consideration of Eq. (57):

$$\boldsymbol{\sigma}_{n+1} = \mathbb{C}_{n+1} : \left(\boldsymbol{\varepsilon}_n + \Delta\boldsymbol{\varepsilon}_{n+1} - \boldsymbol{\varepsilon}^{\mathrm{in}}_n - \Delta\boldsymbol{\varepsilon}^{\mathrm{in}}_{n+1}\right). \tag{64}$$

Now, a nonlinear system of equations, comprising Eqs. (64) and (57)–(60), has been derived and must be solved. Since the solution of this system of equations is performed within a finite element code, we switch from tensor notation to the matrix notation according to Voigt in the following. For this purpose, the stress vectors $\mathbf{s}$ and $\tilde{\mathbf{s}}$, the backstress vector $\mathbf{b}$ and the strain vector $\mathbf{e}$ are introduced:

$$\mathbf{s} = \begin{bmatrix}\sigma_{11} & \sigma_{22} & \sigma_{33} & \sigma_{12} & \sigma_{13} & \sigma_{23}\end{bmatrix}^{\mathrm{T}}, \tag{65}$$

$$\tilde{\mathbf{s}} = \begin{bmatrix}\tilde{\sigma}_{11} & \tilde{\sigma}_{22} & \tilde{\sigma}_{33} & \tilde{\sigma}_{12} & \tilde{\sigma}_{13} & \tilde{\sigma}_{23}\end{bmatrix}^{\mathrm{T}}, \tag{66}$$

$$\mathbf{b} = \begin{bmatrix}\beta_{11} & \beta_{22} & \beta_{33} & \beta_{12} & \beta_{13} & \beta_{23}\end{bmatrix}^{\mathrm{T}}, \tag{67}$$

$$\mathbf{e} = \begin{bmatrix}\varepsilon_{11} & \varepsilon_{22} & \varepsilon_{33} & 2\varepsilon_{12} & 2\varepsilon_{13} & 2\varepsilon_{23}\end{bmatrix}^{\mathrm{T}}. \tag{68}$$

The vectors for the stress deviators, the inelastic or elastic strains, and other incremental entities are formulated and named in an analogous manner. To solve the nonlinear system of equations with the Newton-Raphson method, the equations are reformulated as follows:

$$\mathbf{r}^i_\sigma = \mathbf{0}, \tag{69}$$

$$\mathbf{r}^i_\beta = \mathbf{0}, \tag{70}$$

$$r^i_\Gamma = 0, \tag{71}$$

while introducing the residual quantities $\mathbf{r}^i_\sigma$, $\mathbf{r}^i_\beta$, and r^i_Γ

$$\mathbf{r}^i_\sigma = -\mathbf{e}_{n+1} + \mathbf{e}^{\mathrm{in}}_n + \mathbf{C}^{-1}_{n+1}\mathbf{s}^i_{n+1} + \Delta\mathbf{e}^{\mathrm{in}^i}_{n+1}, \tag{72}$$

$$\mathbf{r}^i_\beta = -\mathbf{b}_n + \mathbf{b}^i_{n+1} - \Delta\mathbf{b}^i_{n+1}, \tag{73}$$

$$r^i_\Gamma = -\Gamma_n + \Gamma^i_{n+1} - \Delta\Gamma^i_{n+1}. \tag{74}$$

Note that $\square^i$ denotes the iteration index. Furthermore, the elasticity stiffness matrix $\mathbf{C}$ and its inverse $\mathbf{C}^{-1}$ in Voigt notation have been introduced. Within the application of the Newton-Raphson method, Eqs. (69)–(71) are linearized, cf. Wriggers (2008):

$$\mathbf{A}^i_{n+1}\Delta\mathbf{p}^{i+1}_{n+1} = -\mathbf{r}^i_{n+1}, \tag{75}$$

whereby the vector $\mathbf{p}^{i+1}_{n+1}$ summarizes the updated values of the primary solution variables, and the vector $\mathbf{r}^i_{n+1}$ comprises the corresponding residual quantities:

$$\mathbf{p}^{i+1}_{n+1} = \begin{bmatrix}\mathbf{s}^{i+1}_{n+1} & \mathbf{b}^{i+1}_{n+1} & \Gamma^{i+1}_{n+1}\end{bmatrix}^{\mathrm{T}}, \tag{76}$$

$$\mathbf{r}^i_{n+1} = \begin{bmatrix}\mathbf{r}^i_\sigma & \mathbf{r}^i_\beta & r^i_\Gamma\end{bmatrix}^{\mathrm{T}}. \tag{77}$$

The solution of Eq. (75) provides the vector of increments $\Delta\mathbf{p}^{i+1}_{n+1}$, which is used to update the stress, the backstress, and the softening variable:

$$\mathbf{p}^{i+1}_{n+1} = \mathbf{p}^i_{n+1} + \Delta\mathbf{p}^{i+1}_{n+1}. \tag{78}$$

The matrix $\mathbf{A}^{i}_{n+1}$ in Eq. (75) contains the derivatives of the residuals with respect to the primary solution variables $\mathbf{s}$, $\mathbf{b}$, Γ, cf. Eisenträger et al. (2018b). The derivatives of the residuals can be calculated based on Eqs. (72)–(74). Since the resulting expressions are lengthy, the equations are not repeated here for the sake of brevity. The interested reader is referred to Eisenträger et al. (2018b), where the derivatives are presented in detail. Next, the system of equations (75) is solved via the Newton-Raphson method. Note that further details on this point can also be found in Eisenträger et al. (2018b); Eisenträger (2018). After solving the system of equations, the primary solution variables are updated based on Eq. (78), such that the current values of the stress $\mathbf{s}_{n+1}$, the backstress $\mathbf{b}_{n+1}$, and the softening variable Γ_{n+1} are known.

3.1.2 Consistent Tangent Operator

Additionally to the update of the primary solution variables, the consistent tangent operator (CTO) must be provided to implement a nonlinear constitutive model into the FEM, cf. Simo and Taylor (1985); Hartmann et al. (1997). As before, if not indicated otherwise, all variables refer to the time step t_{n+1} in the remainder of this section. Let us introduce the matrix $\mathbf{D}$ for the CTO as follows:

$$\mathbf{D} = \left.\frac{\partial \mathbf{s}}{\partial \mathbf{e}}\right|_{n+1}. \tag{79}$$

To determine the derivative of the stresses with respect to the strains, the implicit function theorem is utilized, cf. Ghorpade and Limaye (2010). Consequently, by introducing the implicit function $\mathbf{f}$:

$$\mathbf{f}(\mathbf{s}_{n+1}, \mathbf{b}_{n+1}, \Gamma_{n+1}, \mathbf{e}_{n+1}) = \mathbf{s}_{n+1} - \mathbf{C}_{n+1}\left(\mathbf{e}_{n+1} - \mathbf{e}^{\mathrm{in}}_{n} - \Delta\mathbf{e}^{\mathrm{in}}_{n+1}\right), \tag{80}$$

Eq. (64) is formulated in a matrix notation as follows:

$$\mathbf{f}(\mathbf{s}_{n+1}, \mathbf{b}_{n+1}, \Gamma_{n+1}, \mathbf{e}_{n+1}) = \mathbf{0}. \tag{81}$$

The inelastic strain increment $\Delta\mathbf{e}^{\mathrm{in}}_{n+1}$ in Eq. (80) is obtained while making use of Eqs. (57)–(60). Based on the implicit function theorem, the CTO is computed in the following way:

$$\mathbf{D} = \left.\frac{\partial \mathbf{s}}{\partial \mathbf{e}}\right|_{n+1} = -\left(\frac{\partial \mathbf{f}}{\partial \mathbf{s}_{n+1}}\right)^{-1}\frac{\partial \mathbf{f}}{\partial \mathbf{e}_{n+1}}, \tag{82}$$

whereby the arguments of the implicit function $\mathbf{f}$ are omitted for the sake of brevity. Computing the derivatives based on Eq. (80) results in:

$$\mathbf{D} = \left(\mathbf{A}_1 + \mathbf{C}_{n+1}\frac{\partial \Delta\mathbf{e}^{\mathrm{in}}_{n+1}}{\partial \mathbf{s}_{n+1}}\right)^{-1}\mathbf{C}_{n+1}, \tag{83}$$

while the derivative of the inelastic strain increment with respect to the stress is determined based on Eq. (58):

$$\frac{\partial \Delta\mathbf{e}^{\mathrm{in}}_{n+1}}{\partial \mathbf{s}_{n+1}} = \frac{3}{2}\frac{\Delta t\, f_T(T)}{\tilde{\sigma}_{\mathrm{vM}}}\left[\frac{3}{2}\left(\frac{1}{\tilde{\sigma}_{\mathrm{vM}}}\frac{\partial f_\sigma(\tilde{\sigma}_{\mathrm{vM}})}{\partial \tilde{\sigma}_{\mathrm{vM}}} - \frac{f_\sigma(\tilde{\sigma}_{\mathrm{vM}})}{\tilde{\sigma}^2_{\mathrm{vM}}}\right)\tilde{\mathbf{s}}'\left(\tilde{\mathbf{s}}'\right)^{\mathrm{T}} + f_\sigma(\tilde{\sigma}_{\mathrm{vM}})\left(\mathbf{A}_1 - \frac{1}{3}\mathbf{A}_2\right)\right], \tag{84}$$

with the auxiliary matrices $\mathbf{A}_1$ and $\mathbf{A}_2$:

$$\mathbf{A}_1 = \begin{bmatrix} 1 & 0 & 0 & 0 & 0 & 0 \\ 0 & 1 & 0 & 0 & 0 & 0 \\ 0 & 0 & 1 & 0 & 0 & 0 \\ 0 & 0 & 0 & 1 & 0 & 0 \\ 0 & 0 & 0 & 0 & 1 & 0 \\ 0 & 0 & 0 & 0 & 0 & 1 \end{bmatrix}, \qquad \mathbf{A}_2 = \begin{bmatrix} 1 & 1 & 1 & 0 & 0 & 0 \\ 1 & 1 & 1 & 0 & 0 & 0 \\ 1 & 1 & 1 & 0 & 0 & 0 \\ 0 & 0 & 0 & 0 & 0 & 0 \\ 0 & 0 & 0 & 0 & 0 & 0 \\ 0 & 0 & 0 & 0 & 0 & 0 \end{bmatrix}.$$

Using the commercial FE code ABAQUS, the stress update algorithm, presented in Sect. 3.1.1, and the CTO are implemented into the FEM via a user material (UMAT) subroutine. The accuracy and numerical performance of the implemented constitutive model based on the implicit Euler method have been examined in detail, considering several benchmarks for uniaxial and multiaxial stress and deformation states, cf. Eisenträger et al. (2018b); Eisenträger (2018).

3.2 Explicit Time Integration

3.2.1 Stress Update Algorithm

The current section presents the stress update algorithm of the mixture model based on explicit time integration, i.e. the forward Euler method is applied. In general, the following considerations are in close agreement to the derivations for the implicit Euler method in Sect. 3.1.1. For the time integration of the governing equations based on the explicit Euler method, we apply Eq. (56) to the constitutive equations. If not stated otherwise, all entities refer to the time step t_n in the remainder of this section. As before,

it is assumed that all principal variables are known for the equilibrium state at the time step t_n. Applying the forward Euler method, results in the following system of equations, which is directly formulated in a matrix notation for the sake of brevity:

$$\square_{n+1} = \square_n + \Delta\square_n \qquad \forall \quad \square = \left\{\mathbf{e}, \mathbf{e}^{\text{in}}, T, \mathbf{s}, \mathbf{b}, \Gamma\right\}, \tag{85}$$

$$\Delta\mathbf{e}^{\text{in}}_n = \frac{3}{2}\Delta t\, f_\sigma\left(\tilde{\sigma}_{\text{vM}}\right)\frac{f_T\left(T\right)}{\tilde{\sigma}_{\text{vM}}}\tilde{\mathbf{s}}', \tag{86}$$

$$\Delta\mathbf{b}_n = \frac{1}{G}\frac{\mathrm{d}G}{\mathrm{d}T}\Delta T\mathbf{b} + 2G\frac{\eta_{\text{h}_0}}{1-\eta_{\text{h}_0}}\left(\Delta\mathbf{e}^{\text{in}} - \frac{3}{2}\frac{\Delta\varepsilon^{\text{in}}_{\text{vM}}}{\beta_{\text{vM}_\star}}\mathbf{b}\right), \tag{87}$$

$$\Delta\Gamma_n = C_\Gamma\left[\Gamma_\star\left(\sigma_{\text{vM}}\right) - \Gamma\right]\Delta\varepsilon^{\text{in}}_{\text{vM}}, \tag{88}$$

$$\mathbf{s}_{n+1} = \mathbf{C}_{n+1}\left(\mathbf{e}_n + \Delta\mathbf{e}_n - \mathbf{e}^{\text{in}}_n - \Delta\mathbf{e}^{\text{in}}_n\right). \tag{89}$$

Note that in contrast to the implicit time integration, the application of an explicit method does not result in a nonlinear system of equations. Instead, Eqs. (85)–(89) directly provide the values of the primary solution variables, i.e. $\mathbf{s}_{n+1}$, $\mathbf{b}_{n+1}$, and Γ_{n+1}, with respect to the current time step t_{n+1}.

3.2.2 Consistent Tangent Operator

Despite applying an explicit time integration method, the CTO must be provided as well to implement a nonlinear constitutive model into the FEM. Following an analogous procedure as in Sect. 3.1.2 results in the following expression for the CTO in matrix notation:

$$\mathbf{D} = \left(\mathbf{A}_1 + \mathbf{C}_{n+1}\frac{\partial\Delta\mathbf{e}^{\text{in}}_n}{\partial\mathbf{s}_n}\right)^{-1}\mathbf{C}_{n+1}, \tag{90}$$

In contrast to Eq. (83), the derivative of the inelastic strain increment with respect to the stress is calculated with respect to the time step t_n, such that Eq. (84) is also evaluated with respect to the step t_n. The stress update algorithm in Sect. 3.2.1 and the CTO for explicit time integration are also implemented via the UMAT subroutine into ABAQUS. However, as it has already been discussed at the beginning of Sect. 3, explicit integration methods are only *conditionally* stable, such that if the time increments exceed a certain threshold, the so-called "critical time step size", the solution might become unstable. In order to circumvent this issue, the UMAT subroutine compares the current time increment to a critical time step size Δt_{crit} and provides a warning message if the current time step exceeds the critical value. To estimate the critical time step size for the mixture model, we have adopted the approach presented in Cormeau (1975), where the critical time step size is derived for a related constitutive approach, i.e. a von Mises viscoplasticity model with zero yield stress, suitable for the creep analysis of metals and employing similar stress and temperature response functions as presented in Sect. 2.2. Based on Cormeau (1975), the critical time step size is determined as follows:

$$\Delta t_{\text{crit}} = \frac{2}{3Ga_\sigma m_\sigma f_T(T)}\tilde{\sigma}_{\text{vM}}^{1-m_\sigma} \tag{91}$$

4 Finite Element Analysis of a Steam Turbine Rotor

4.1 Numerical Model: Procedures, Mesh, and Boundary Conditions

The thermo-mechanical behavior of the steam turbine rotor is analyzed within a partly coupled finite element analysis, using the commercial FE code ABAQUS. In a first step, a thermal analysis is conducted in order to obtain the temperature field based on the heat transfer due to the inhomogeneous and instationary steam temperatures. Afterwards, the temperature distribution is utilized as input for the subsequent structural analysis with the binary mixture model, which provides the resulting strain and stress fields. This type of partly coupled thermo-mechanical analysis is frequently applied, particularly to avoid the high computational effort of a fully coupled analysis, cf. e.g. Nayebi et al. (2012); Sun et al. (2013); Benaarbia et al. (2018). To the knowledge of the authors, the results of a fully coupled thermo-mechanical analysis of a turbine rotor have not been presented in literature yet. Furthermore, it is questionable whether the mechanical deformations exert a significant influence on the temperature field assuming moderate inelastic deformations in components in practice. However, also due to the lack of experimental data and measurements under operating conditions, this issue remains an open question. Future research could therefore concentrate on the development of a fully coupled thermo-mechanical model and the comparison of partly and full coupled approaches for the analysis of turbine rotors.
In the present analysis, all computations for the structural analysis are conducted twice, considering explicit and implicit time integration, as described in Sect. 3.1 and 3.2. Both time integration methods are critically examined with respect to the involved computational effort as well as the accuracy in Sect. 4.2. In the following two sections, the employed FE models, i.e. the meshes as well as the boundary conditions, are described both for the thermal and structural analysis.

4.1.1 Thermal Analysis

Figure 2 presents the FE model with the boundary conditions for the thermal analysis of the steam turbine rotor. The top left picture shows the geometry of the rotor, which refers to a real component used in power plants. Note that the geometry data has

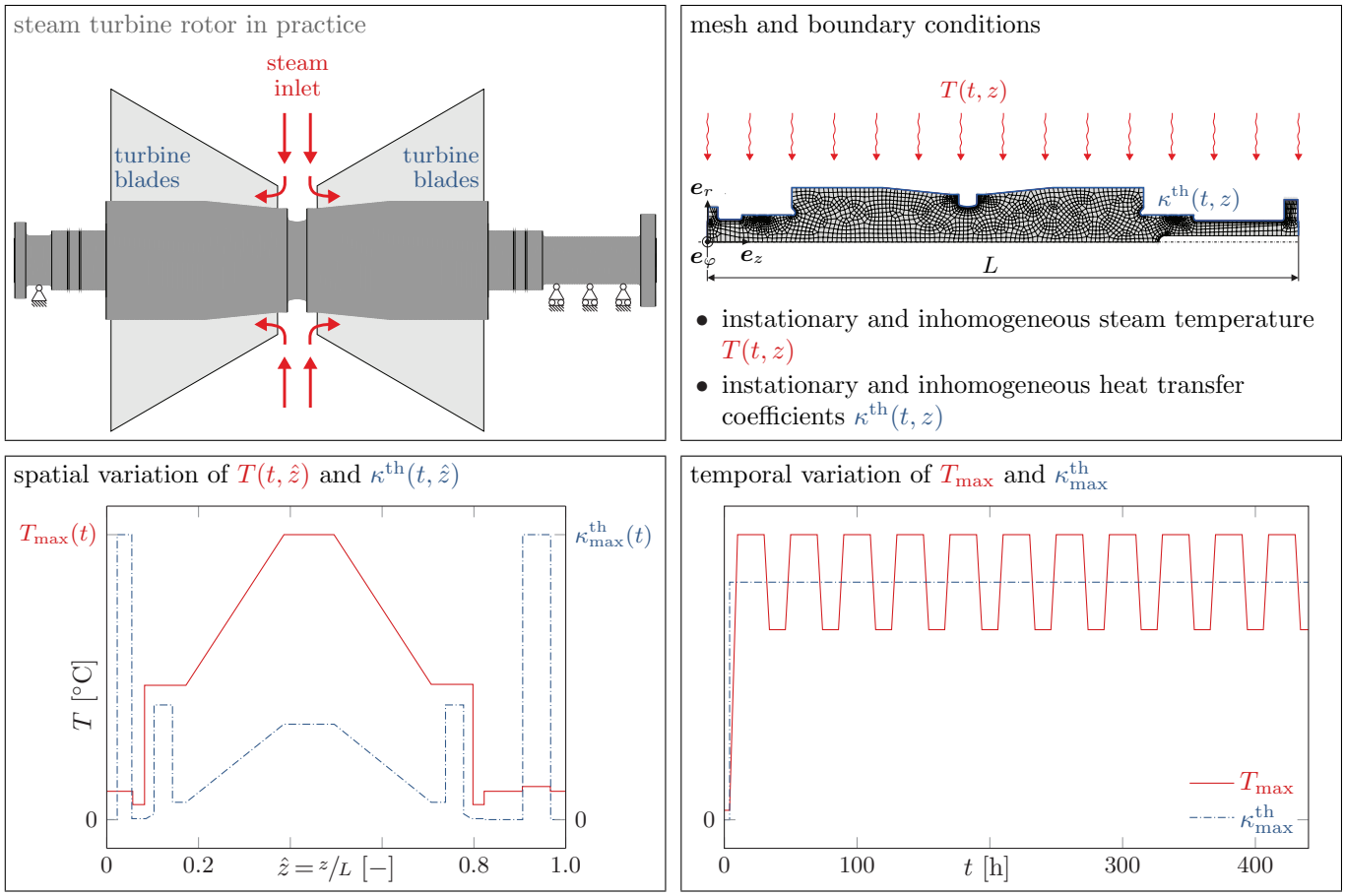

Fig. 2: Finite element model, mesh, and boundary conditions for the thermal analysis.

been provided by Siemens AG, Power and Gas Division, MÃijlheim an der Ruhr, Germany. Furthermore, Siemens AG has also given advice concerning the applied thermo-mechanical boundary conditions in order to account for the operating conditions in power plants. As depicted in the top left picture in Fig. 2, the rotor is mounted at the left and right-hand side. In the center, hot steam is lead in and redirected towards the turbine blades. Note that the blades themselves are not included in the thermal analysis, cf. the top right picture, to reduce the computational effort.

The axisymmetric mesh is shown in the top right picture in Fig. 2. From the ABAQUS element library, the 8-node heat transfer element DCAX8 with quadratic shape functions has been chosen. The depicted mesh comprises 2391 elements and 7636 nodes. In order to simulate the heat transfer based on the prescribed outer steam temperature T over the outer surface of the rotor (marked in blue color in the top right picture) inside the rotor, the ABAQUS user subroutine FILM is utilized. Thereby, we prescribe the steam temperature and the heat transfer coefficient κ^{th}, which both depend on the time and change along the longitudinal coordinate z of the rotor. The dependence of the steam temperature and the heat transfer coefficient on the normalized longitudinal coordinate $\hat{z}$ is illustrated in the bottom left picture. As to be expected, the outer temperature attains its maximum near the steam inlet of the rotor. Note that cooling systems are installed near the mountings such that the temperature decreases and the heat transfer coefficient increases at the left and right-hand side of the rotor.

Finally, the temporal variation of the maximum steam temperature and heat transfer coefficient is shown in the bottom right diagram. As the graph for the maximum temperature shows, a total of 11 thermal cycles is taken into account. The first cycle represents a cold start with a significant increase in temperature. After reaching the maximum temperature, the temperature is held constant over 20 hours (“holding stage”). Afterwards, the temperature decreases to an intermediate level and is again held constant over 12 hours. Finally, the temperature increases again from the intermediate level until the maximum is reached (warm start). Thus, 11 cycles, including one cold start and 10 warm starts, are taken into account, which allows for a comparison of the different starting procedures as well as the analysis of the cyclic behavior. In total, the simulated time span accounts for 446 hours. In contrast to the varying temperature, the maximum heat transfer coefficient $\kappa^{\mathrm{th}}_{\max}$ increases only at the initial start to account for the large differences in temperatures and heat transfer. Afterwards, the maximum heat transfer coefficient is assumed to be constant due to the intermediate temperature differences in the following cycles. Note that the temporal variation of the lower levels of temperature and heat transfer coefficient, cf. the bottom left diagram, is described by scaling the lower levels proportionally depending on the current maximum value.

4.1.2 Structural Analysis

The FE model and the boundary conditions for the structural analysis are explained in Fig. 3. As before, the top left picture displays the steam turbine rotor in practice. The top right picture shows the finite element mesh, whose nodal positions and topology are

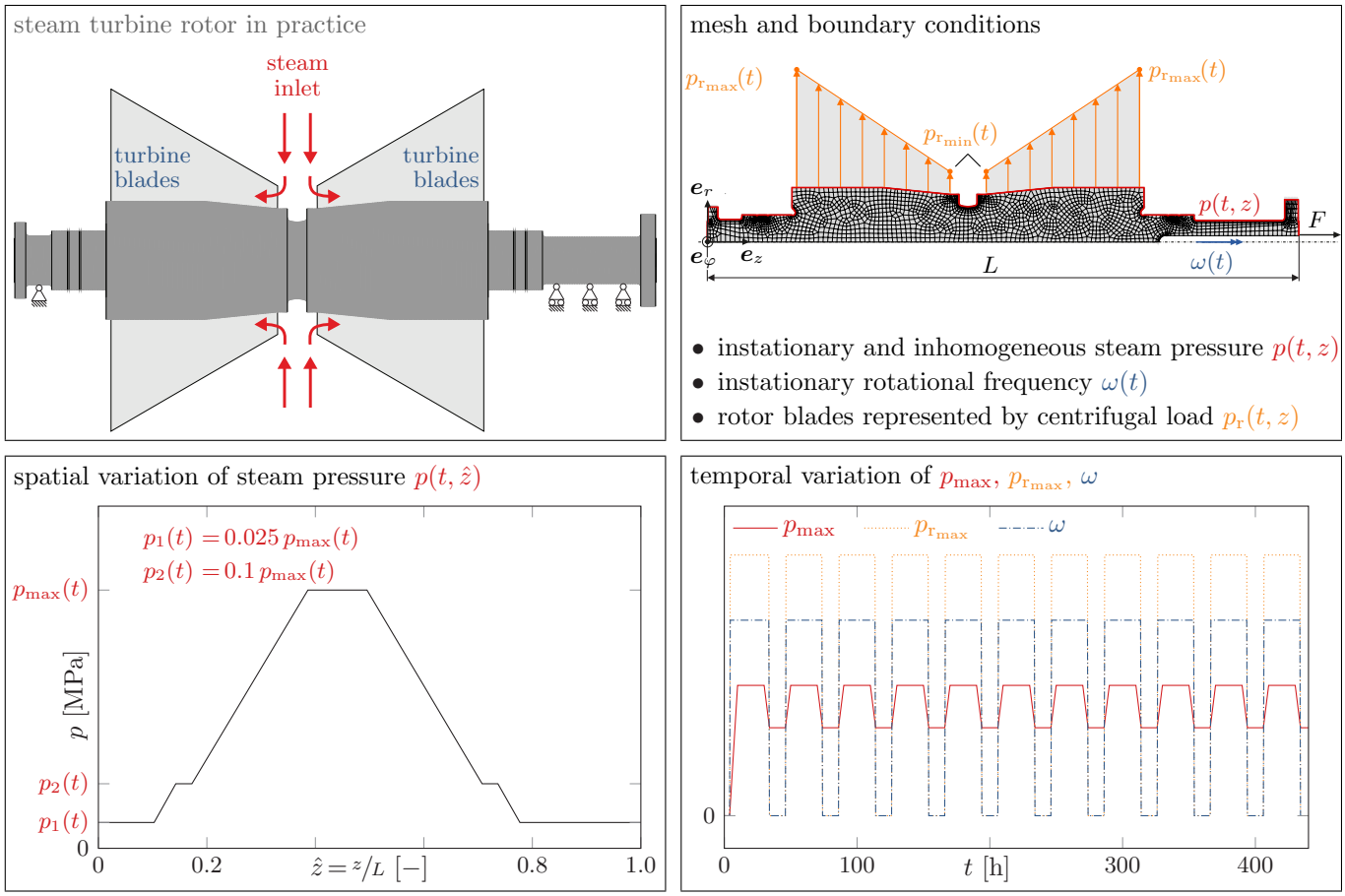

Fig. 3: Finite element model, mesh, and boundary conditions for the structural analysis.

adopted from the thermal analysis, although a different element, suitable for structural analysis, is chosen, i.e. the element CAX8 from ABAQUS' element library. Like the heat transfer element DCAX8, the quadrilateral element CAX8 features 8 nodes and uses quadratic shape functions.

As already pointed out, the temperature field obtained in the preceding thermal analysis is imported as thermal boundary condition in the structural analysis. Furthermore, the instationary and inhomogeneous steam pressure p is prescribed along the outer surface of the rotor marked in red, cf. the top right picture of Fig. 3. Similar to the steam temperature, cf. Fig. 2, the variation of the steam pressure with respect to the normalized longitudinal coordinate $\hat{z}$ of the rotor is given in the bottom left picture of Fig. 3. As one would expect, the spatial variation of the steam pressure is in close agreement with the spatial change of temperature, cf. the bottom left diagram in Fig. 2. Note that the change of the maximum steam pressure p_{max} with respect to time is given in the bottom right diagram in Fig. 3. In analogy to the proportional scaling of the temperature levels, the lower levels of the steam pressure p_1 and p_2 are adapted as well such that the ratios $p_1/p = 0.025$ and $p_2/p = 0.1$ remain constant over time.

In addition, a time-dependent rotational frequency ω is provided to simulate the various starting and shut-down procedures, cf. the pictures in the right-hand side in Fig. 3. In order to reduce the involved computational effort, the rotor blades are not modeled explicitly. Instead, they are represented by the centrifugal load p_r, which varies linearly from the minimum value $p_{r_{min}}$ at the steam inlet to its maximum $p_{r_{max}}$, in order to account for the increasing length of the rotor blades. Note that this representation of the blades by centrifugal loads is a commonly applied procedure, cf. Wang et al. (2016); Zhu et al. (2017); Benaarbia et al. (2018). To complete the overview on the mechanical boundary conditions, the maximum centrifugal load $p_{r_{max}}$ is shown depending on time in the bottom right diagram in Fig. 3.

4.2 Explicit and Implicit Time Integration

Before the obtained temperature, stress, and strain fields in the rotor are presented in detail in Sect. 4.3, we will compare the performance of the explicit and implicit Euler method for time integration. Note that this is rarely done with respect to a complex simulation of a realistic component such as a steam turbine rotor, although reducing the involved computational costs in practical simulations is of crucial importance, particularly if instationary and cyclic loads are taken into account. In order to compare both time integration methods, several structural analyses are conducted using the ABAQUS implementations of the time integration methods presented in Sect. 3. ABAQUS' automatic time stepping algorithm is used, and the maximum time step size Δt_{max} is varied systematically, i.e. $\Delta t_{max} = \{0.10\,\text{h}, 0.05\,\text{h}, 0.01\,\text{h}\}$, both for implicit and explicit time integration, such that a total of six different structural simulations is conducted. All structural simulations are based on the same temperature field, which is obtained in the preceding heat transfer analysis with lowest maximum time step size $\Delta t_{max} = 0.01\,\text{h}$. For all simulations, a Windows 7 (64 bit) desktop computer with Intel Core i7-58205 processor (clock rate 3.30 GHz) and 16 GB RAM is used.

Figure 4 comprises all required data for the comparison of the time integration methods. The top diagram shows the von Mises

stress at the point P_1, which has been chosen due to its particular position at notch root directly under the steam inlet, as indicated in the sketch in the background of Fig. 4. In the diagram, the von Mises stress is displayed depending on the simulated time, which covers all 11 cycles. Furthermore, the von Mises stress is normalized with respect to the maximum equivalent stress $\sigma_{\mathrm{vM}_{\max}}^{\mathrm{P1}}$ at the point P_1. Note that since all FE simulations yield very similar results such that the different curves could not be distinguished with the naked eye, here we only show the result of one representative simulation, i.e. the analysis involving implicit integration with lowest maximum time step size $\Delta t_{\max} = 0.01\,\mathrm{h}$ for the sake of illustration. The curve shows a total of 22 significant local stress maxima, whereby two maxima each refer to one cycle including start-up (first maximum), holding phase, and shut-down (second maximum). The presented curve is extracted for all six structural simulations and serves as basis to define the von Mises stress error Δ_{vM} as follows:

$$\Delta_{\mathrm{vM}} = \frac{\int \left(\sigma_{\mathrm{vM}}^{\mathrm{ref}} - \sigma_{\mathrm{vM}}^{\mathrm{num}}\right)^2 \mathrm{d}t}{\int \left(\sigma_{\mathrm{vM}}^{\mathrm{ref}}\right)^2 \mathrm{d}t}, \tag{92}$$

whereby the variable $\sigma_{\mathrm{vM}}^{\mathrm{num}}$ is replaced by the simulation results for explicit and implicit integration considering the variations in time stepping:

$$\sigma_{\mathrm{vM}}^{\mathrm{num}} = \left\{\sigma_{\mathrm{vM}}^{INT}\left(\Delta t_{\max} = 0.10\,\mathrm{h}\right), \sigma_{\mathrm{vM}}^{INT}\left(\Delta t_{\max} = 0.05\,\mathrm{h}\right), \sigma_{\mathrm{vM}}^{INT}\left(\Delta t_{\max} = 0.01\,\mathrm{h}\right)\right\} \qquad \forall INT = \{\mathrm{exp}, \mathrm{imp}\}\,.$$

In addition, $\sigma_{\mathrm{vM}}^{\mathrm{ref}} = \sigma_{\mathrm{vM}}^{\mathrm{imp}}\left(\Delta t_{\max} = 0.01\,\mathrm{h}\right)$ holds, i.e. the simulation results obtained with implicit time integration and smallest time steps are used as reference solution. The superscripts $\square^{\mathrm{imp}}$ and $\square^{\mathrm{exp}}$ indicate variables obtained via implicit and explicit time integration, respectively. Note that the integrals in Eq. (92) are evaluated numerically using the trapezoidal rule. To ensure equal time steps in the numerical solution $\sigma_{\mathrm{vM}}^{\mathrm{num}}$ and the reference solution $\sigma_{\mathrm{vM}}^{\mathrm{ref}}$ for applying the trapezoidal rule, the values of the numerical solution are interpolated linearly to the time steps provided by the reference solution.

The bottom left diagram in Fig. 4 shows the above defined stress error depending on the total CPU time t_{CPU} both for explicit and implicit time integration. In addition, the corresponding data is given on the right-hand side of Fig. 4 in tabular form. As one would expect, a direct correlation is found between the prescribed maximum time step size $\Delta t_{\max}$ and the required computational time t_{CPU}, i.e. the lower the maximum time step size, the longer the computational time. Furthermore, the tables show that both methods converge, i.e. the stress error decreases with decreasing time step size. Whereas we can only observe a slight reduction in the stress error for implicit integration, the stress error for explicit integration decreases significantly until a similar accuracy as for implicit integration is reached. Note that since the simulation with implicit integration and lowest maximum time step size has been chosen as reference solution, the corresponding stress error is exactly zero. Furthermore, one should point out the overall small size of the stress error, which never exceeds 0.1%.

Interestingly, we cannot observe a significant difference in computational times, especially in case of a coarser time stepping, between the implicit and explicit Euler methods. Although implicit integration requires the solution of a nonlinear system of equations, which increases the computational costs in general, as discussed at the beginning of Sect. 3, this increase in computational time is negligible for the discussed problem, i.e. the thermo-mechanical analysis of a steam turbine rotor. Note that the discussed increase in computational time is only significant for a very fine time stepping ($\Delta t_{\max} = 0.01\,\mathrm{h}$), which is futile for implicit integration due to the negligible increase in accuracy. Overall, we recommend using the implicit Euler method for the considered initial boundary value problem for two main reasons: Firstly, we can obtain a high level of accuracy in results already with a relatively coarse time stepping, which results in a reasonable computational time. Secondly, one should consider the unconditional stability of implicit methods, which is a significant advantage compared to explicit methods, cf. the discussion at the beginning of Sect. 3. On the other hand, the implementation of implicit time integration methods requires more effort compared to the straightforward formulation of explicit methods, compare Sect. 3.1 and 3.2. One should take this into account while choosing the time integration method: if few changes to the constitutive model are to be expected, implicit integration methods should be preferred. However, if more flexibility is required and changes must be implemented quickly, explicit integration methods are the right choice. Last but not least, we would like to point out that the previous considerations hold for the presented analysis of the steam turbine rotor. One should keep this in mind while transferring the previous conclusions to other initial boundary value problems. Furthermore, all statements hold only for the implicit and explicit Euler method.

4.3 Results

In the following, we will discuss various results of the thermo-mechanical finite element analysis of the rotor. Since the previous section has shown that the structural analysis using implicit time integration for the evolution equations in combination with the coarsest time stepping ($\Delta t_{\max} = 0.10\,\mathrm{h}$) yields accurate results while demanding only for a relatively low CPU time, we will focus on this particular analysis in the following.

Figure 5 shows contour plots of the temperature and normalized von Mises stress in the rotor at two particular points in time. The first point in time under consideration ($t = 10\,\mathrm{h}$) refers to the highest temperature difference $|T_{\mathrm{A}} - T_{\mathrm{B}}|$, which occurs after heating-up in the cold start. Note that T_{A} represents the temperature at point A at notch root at the outer surface of the rotor, as indicated in Fig. 5. The variable T_{B} denotes the temperature at point B, which features the same longitudinal position as point A, but is located at the axis of rotation, i.e. inside the rotor. The second point in time ($t = 30\,\mathrm{h}$) marks the end of the holding stage during the first cycle. Moreover, the top picture in Fig. 5 depicts both temperatures depending on time. One can distinguish the 11 cycles clearly. Note that the graph with respect to the temperature T_{B} is slightly shifted in positive direction of the time axis. Furthermore, the highest temperature at point B is lower than the maximum temperature T_{A}. Both observations can be explained

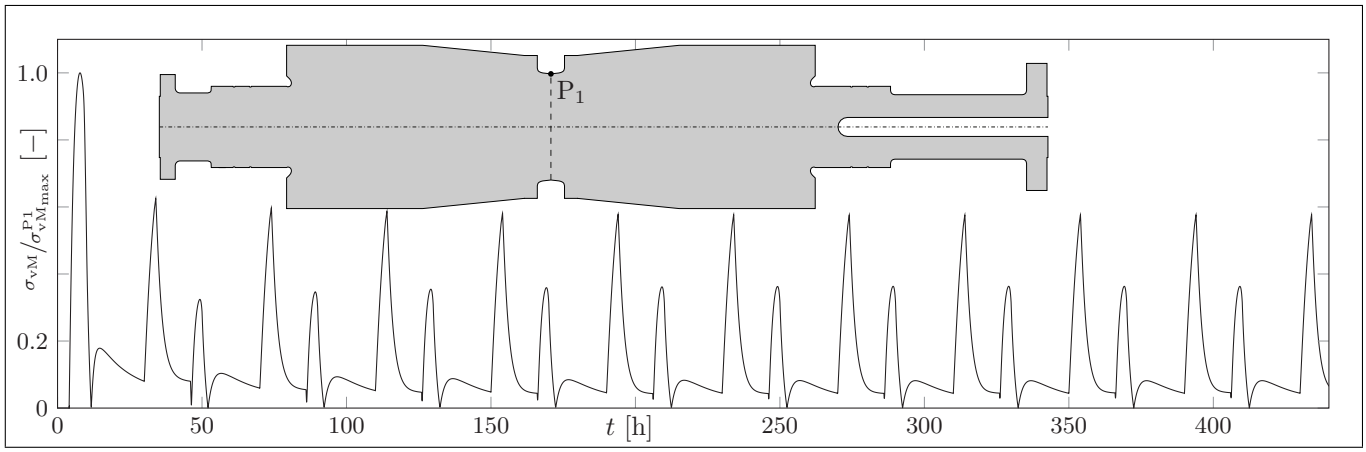

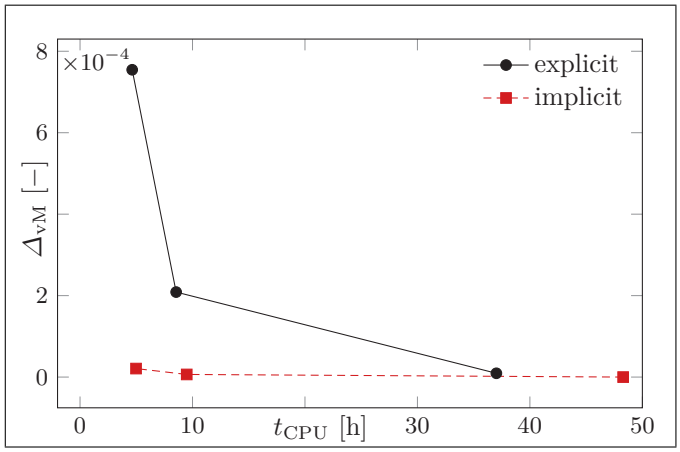

performance of explicit time integration

#	$\Delta t_{\max}$ [h]	t_{CPU} [h]	Δ_{vM} [%]
1	0.10	4.637	0.07545
2	0.05	8.546	0.02087
3	0.01	37.019	0.00093

performance of implicit time integration

#	$\Delta t_{\max}$ [h]	t_{CPU} [h]	Δ_{vM} [%]
1	0.10	4.979	0.00209
2	0.05	9.488	0.00065
3	0.01	48.291	0.00000

Fig. 4: Comparison of explicit and implicit time integration methods. Top: Normalized von Mises stress at point P_1 vs. time. Bottom left: von Mises stress error vs. CPU time. Bottom right: CPU times and von Mises stress error as tabular data.

by the interior position of point B and the relatively slow heat transfer over the outer surface into the rotor. In addition, the chosen points in time are indicated by the red ($t = 10\,\mathrm{h}$) and blue ($t = 30\,\mathrm{h}$) vertical lines in the top picture in Fig. 5.

After 10 h, i.e. at the end of the heating-up and before the beginning of the holding stage, the highest absolute temperature difference between points A and B is attained (217 K). The two contour plots below the top picture refer to this point in time. It is worth noting that the two different starting procedures influence the temperature and stress fields significantly. Whereas the maximum temperature difference during the cold start accounts for 217 K, the highest temperature difference during the subsequent warm starts is significantly lower (112 K at $t = 50\,\mathrm{h}$, for example). In addition, one observes that during heating-up (and cooling-down) the temperature gradient is mainly effective in radial direction. Contrarily, in holding stage temperatures change primarily in longitudinal direction, as can be seen in the fourth picture from the top. Moreover, the large temperature differences during the cold start induce very high stresses in the rotor, cf. the third picture in Fig. 5. As one can observe, high stresses affect the rotor blade area, i.e. the part of the upper surface of the rotor, where the rotor blades are mounted, cf. Fig. 3. This is an issue of high importance since steam turbine rotors usually have several notches in this area to mount the rotor blades. Due to the stress concentration at the notches, the actual stresses in this area could exceed the results presented in this paper. These findings are also confirmed by Wang et al. (2016), where it is demonstrated that the total damage in the rotor concentrates near the blade grooves as well as the steam inlet notch zone. Last but not least, the bottom picture in Fig. 5 shows the contour plot of the normalized von Mises stress at the end of the holding stage in the first cycle ($t = 30\,\mathrm{h}$). Since the temperature difference accounts for only 13 K, the stresses in holding stage are significantly reduced compared to the stresses in the rotor after the cold start.

Based on the obtained contour plots of the von Mises stress in Fig. 5, the three critical points P_1, P_2, and P_3 have been chosen, cf. also the sketch in Fig. 6. While the first two points are located in the central notch at the steam inlet of the rotor, the third point is at the outer surface in the rotor blade area. Figure 6 shows the normalized von Mises stress in these points over time. It becomes obvious that the absolute highest stresses occur during the heating-up in cold start ($4\,\mathrm{h} \leq t \leq 10\,\mathrm{h}$). During the subsequent cycles, i.e. the warm starts, the stresses in cooling-down stage are significantly higher than the corresponding stresses while heating-up, which is due to the relatively fast cooling-down of the steam turbine rotor. Furthermore, we can observe a continuous decrease in the stress maximum in all three specific points throughout the cycles. This behavior is attributed to softening, which is taken into account by the employed mixture model. After all, the point P_2 is most critical because the highest stresses occur at this location. Therefore, the subsequent considerations will focus on this point.

Next, stress and strain components are analyzed at the point P_2. While Fig. 7 displays the normalized stresses and strains at this point over time during the first two cycles only, Fig. 8 provides information on the same variables over the entire computed time, i.e. 11 cycles. The tangential, the circumferential, and the normal components are given with respect to the displayed coordinate

system in the sketch in the top diagram of Fig. 7. Note that these components also represent the principal stresses and strains at the point P_2. Figure 7 provides a detailed view of the first two cycles. We can observe that the absolute highest stresses and strains occur during the heating-up in the cold start (4 . . . 10 h). Whereas the rotor is compressed during the cold and warm starts, stresses and strains are in tensile regime during cooling-down, e.g. at $t \approx 35$ h and $t \approx 75$ h. As has also been stated before, starting with the second cycle (the first warm start), the stresses during cooling-down ($t \approx 75$ h) exceed the corresponding stresses during heating-up ($t \approx 50$ h). Moreover, the stresses decrease constantly during the holding stage (15 . . . 30 h), while the strains increase simultaneously. This indicates creep and relaxation, which are to be expected due to the constant operating conditions during holding stage.

Figure 8 displays the same variables over all 11 cycles. The top diagram clearly shows a slight, but continuous decrease in the maximum values of the circumferential and tangential stresses throughout all cycles. Once more, this decrease in the stress amplitude reveals the occurrence of softening in the material. In addition, the lower diagram provides information on the dependence of the normalized mechanical strains on time. Analogously to the stress components, we can observe a continuous

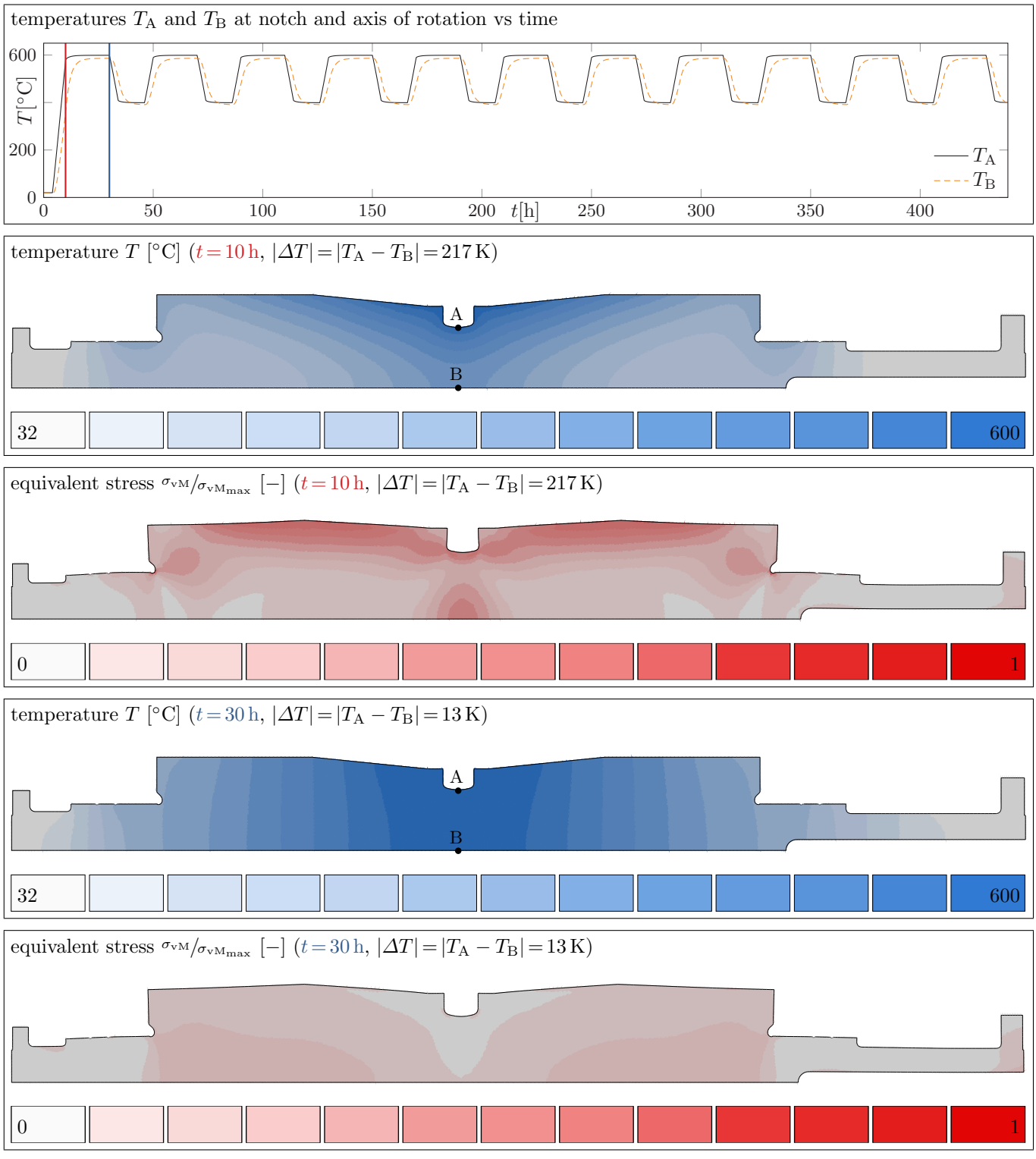

Fig. 5: Contour plots of temperature and normalized von Mises stress in the rotor after 10 h (cold start) and 30 h (holding stage).

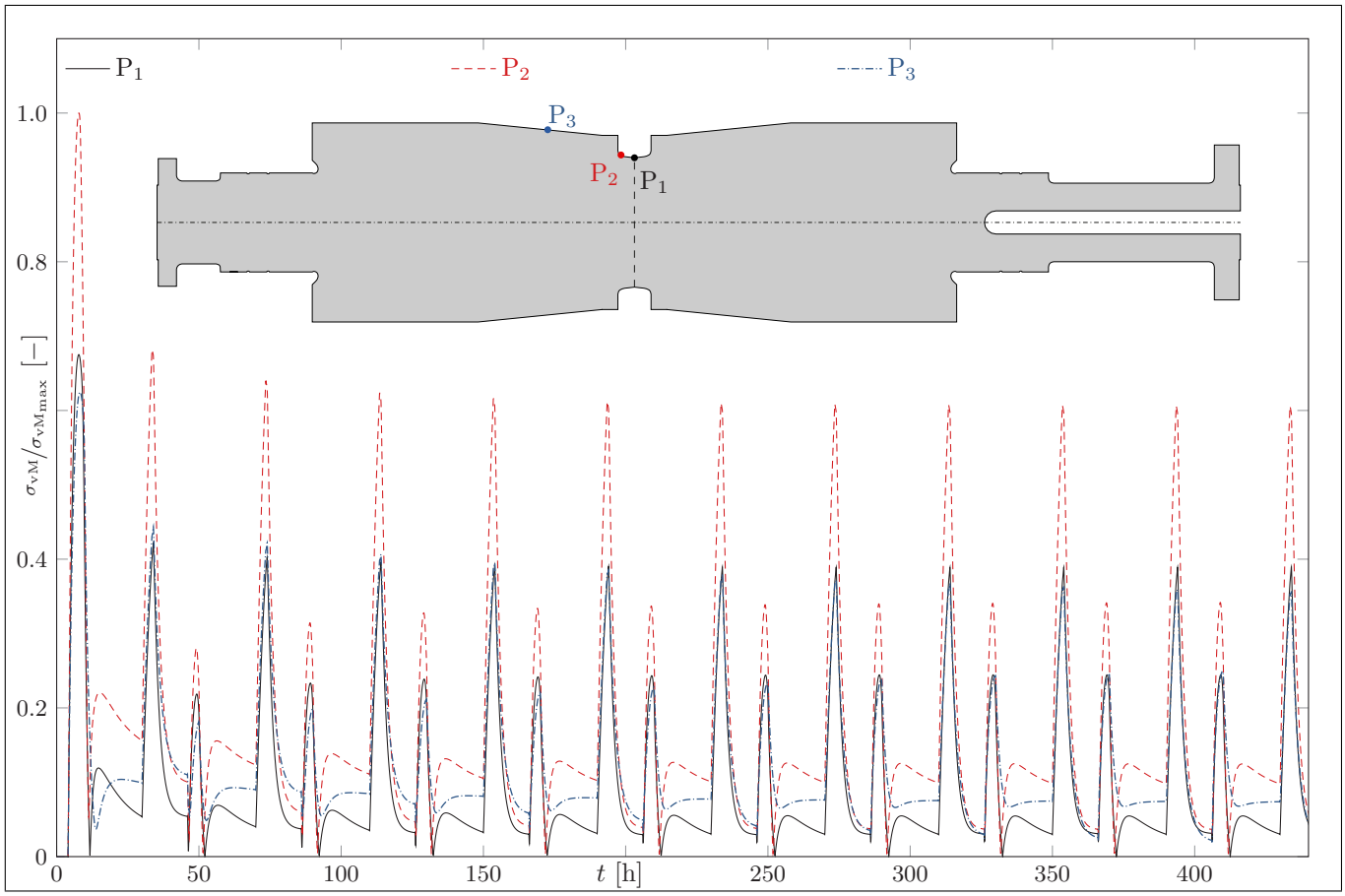

Fig. 6: Normalized von Mises stress in the rotor at three specific points on the steam turbine rotor over time.

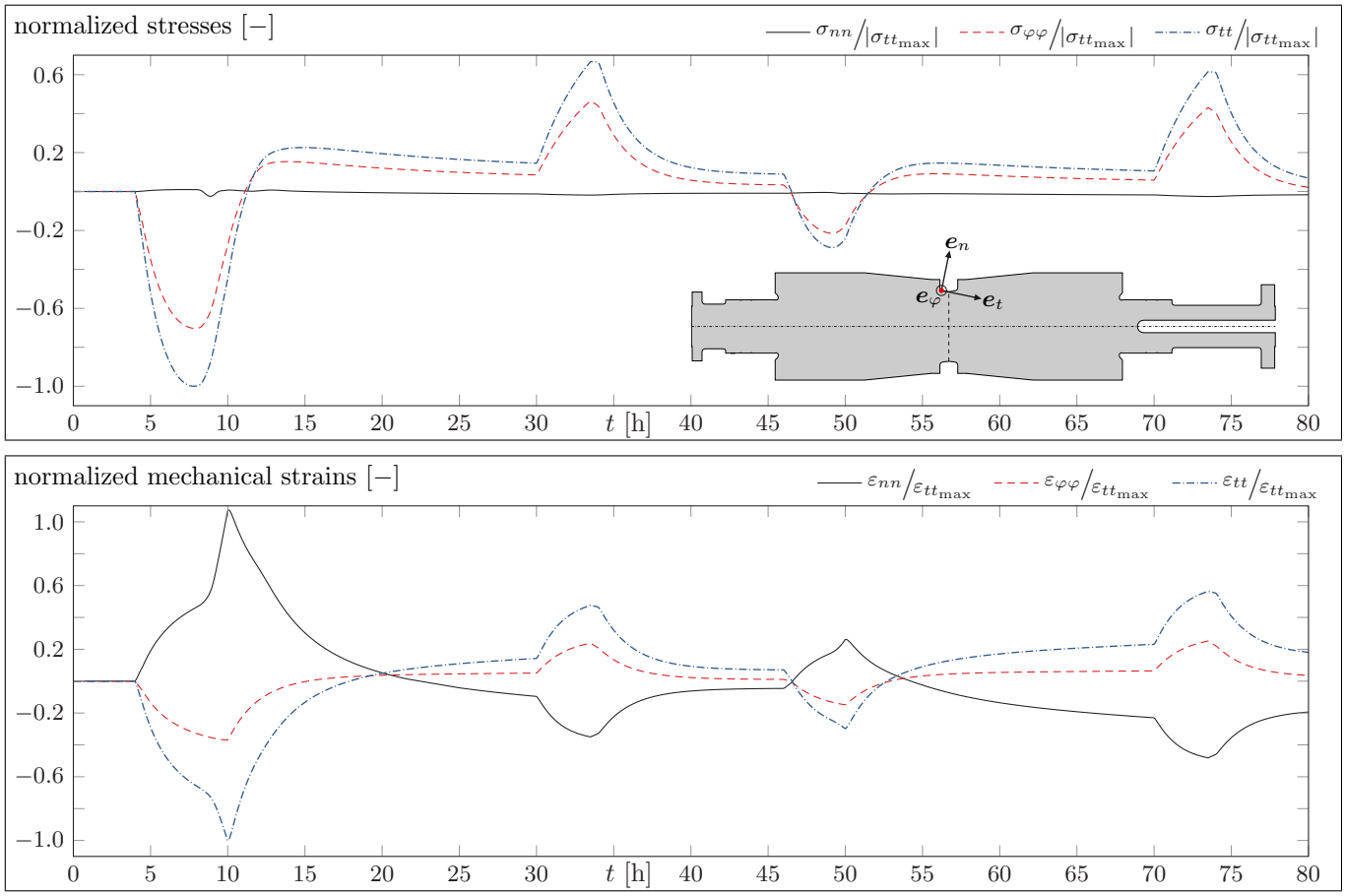

Fig. 7: Normalized stresses and strains at the Point P_2 over time during the first two cycles.

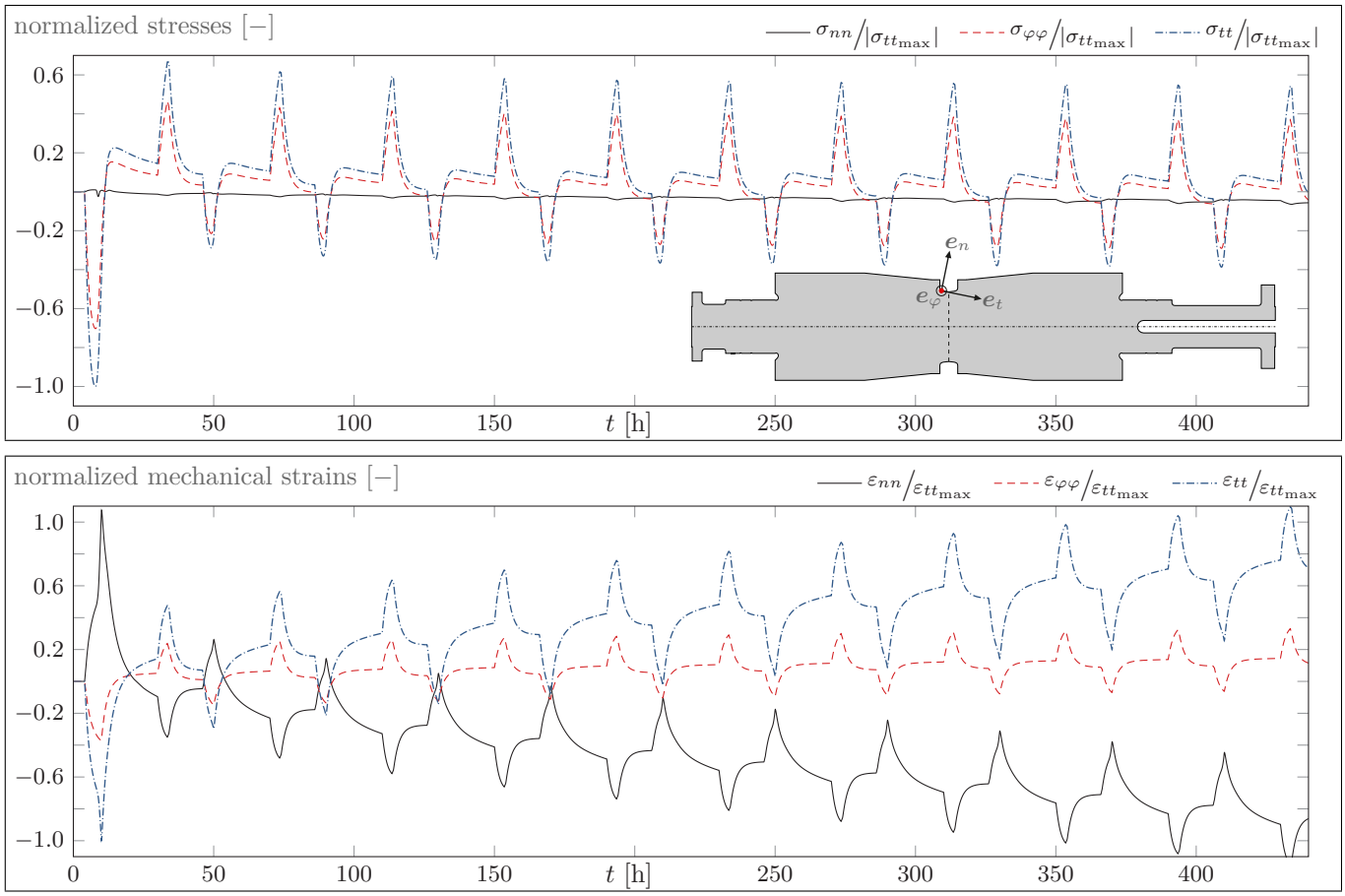

Fig. 8: Normalized stresses and strains at the Point P_2 over time during all 11 cycles.

increase in the maximum tangential and circumferential strains as well as a steady decrease in the minimum values of the normal strain. Thus, the absolute strain values increase during the cycles, and the steam turbine rotor is affected by ratcheting due to the cyclic loads. Note that qualitatively similar simulation results with respect to the stresses and strains have been obtained in Naumenko et al. (2011b); Eisenträger (2018), while analyzing a rotor with idealized geometry.

5 Summary and Outlook

The contribution at hand has presented results of a thermo-mechanical analysis of a steam turbine rotor using a mixture model. The mixture model has been chosen because it provides a robust description of the complex mechanical behavior of high-chromium heat-resistant steels, including rate-dependent inelasticity, (kinematic) hardening, and softening. Furthermore, the model offers three advantages to other approaches: a small number of parameters, the calibration based on simple macroscopic material tests, and its applicability to wide ranges of stress and temperature. Note that the mixture model results in a coupled system of three evolution equations with respect to the inelastic strain, a backstress, and a softening variable. In order to solve this system numerically while implementing the mixture model in the FE code ABAQUS, the current paper applied both the implicit and explicit Euler method and provided detailed information on the derivations of the corresponding stress update algorithms and the consistent tangent operators. This revealed one major advantage of explicit integration methods compared to implicit approaches, i.e. the straightforward implementation of explicit integration methods, which requires significantly less effort in transforming the governing equations compared to implicit approaches.

Next, the paper demonstrated the applicability of the mixture model to a complex thermo-mechanical problem by analyzing a steam turbine rotor with complicated geometry in step with actual practice. Special emphasis was put on the accurate description and close-to-practice implementation of the boundary conditions. Within the preceding thermal analysis with ABAQUS, the temperature field in the rotor was obtained based on the prescribed instationary steam temperatures and heat transfer coefficients. The temperature distribution served as input for the subsequent structural analysis with the mixture model. Furthermore, the simulation covered 11 thermo-mechanical cycles to account for the creep-fatigue loads in real power plant components.

Afterwards, the numerical performance of the explicit and implicit Euler method has been examined in detail by varying the time step sizes systematically. Especially for coarser time stepping, a significant difference in computational times could not be observed. Furthermore, it has been found that both methods result in small stress errors. For the considered boundary value problem, we recommended the implicit Euler method due to two reasons: a high level of accuracy in results, while requiring an acceptable amount of computational time, and the unconditional stability of implicit integration. However, one should keep in mind that the application of implicit methods requires significantly more effort in deriving the equations such that explicit integration schemes should be preferred in cases of frequent changes in the constitutive model.

Finally, we focused on the simulation referring to the largest time step (0.10 h) based on implicit time integration and discussed the corresponding results in detail, with special emphasis on the influence of the different starting procedures (warm and cold starts). It was found that the highest temperature gradients in the rotor occurred in radial direction directly after the cold start. Furthermore, the maximum temperature gradient during the cold start significantly exceeded the highest temperature difference during the subsequent warm starts (217 K in comparison to 112 K, respectively). Consequently, the large temperature differences during the cold start induce significantly higher stresses in the rotor, compared to the stress state during the warm starts. Furthermore, it has been found that particularly in the rotor blade area high stresses occurred, which should be taken into account in a lifetime assessment of a steam turbine rotor. Throughout the thermo-mechanical cycling, the steam turbine rotor is affected both by softening and ratcheting, which is accounted for by the binary mixture model.
Thus, the presented constitutive model provides a robust description of the mechanical behavior of steam turbine rotors. The obtained stress and strain fields could serve as a basis for a subsequent damage analysis to assess the lifetime of power plant components under realistic boundary conditions. Since it is possible to extend the binary mixture model by a damage variable, cf. Naumenko et al. (2011a), this will be the subject of a forthcoming paper. Additionally, one should consider the application of extrapolation techniques to the presented analysis of the steam turbine rotor such that one could predict the long-term mechanical behavior based on the simulation of only a few initial thermo-mechanical cycles. Due to the involved computational costs, this represents an issue of high importance, and the accuracy of proposed extrapolation techniques should be examined carefully.

Acknowledgment

The authors would like to thank Dr. Yevgen Kostenko (Siemens AG, Power and Gas Division, MÃijlheim an der Ruhr, Germany) for providing all required data concerning the geometry as well as the boundary conditions and loads of the steam turbine rotor. Furthermore, the authors are grateful for the continuous advice and helpful discussions with Dr. Kostenko.

References

R. Agamennone, W. Blum, C. Gupta, and J. K. Chakravartty. Evolution of microstructure and deformation resistance in creep of tempered martensitic 9–12%Cr–2%W–5%Co steels. *Acta Materialia*, 54(11):3003–3014, 2006. doi: 10.1016/j.actamat.2006.02.038.

S. Alsagabi, T. Shrestha, and I. Charit. High temperature tensile deformation behavior of Grade 92 steel. *Journal of Nuclear Materials*, 453(1-3):151–157, 2014. doi: 10.1016/j.jnucmat.2014.06.033.

P. J. Armstrong and C. O. Frederick. A Mathematical Representation of the Multiaxial Bauschinger Effect. Technical report, Berkeley Nuclear Laboratories, 1966.

R. J. Atkin and R. E. Craine. Continuum theories of mixtures: basic theory and historical development. *The Quarterly Journal of Mechanics and Applied Mathematics*, 29(2):209–244, 1976. doi: 10.1093/qjmam/29.2.209.

T. Barkar and J. Ågren. Creep simulation of 9–12% Cr steels using the composite model with thermodynamically calculated input. *Materials Science and Engineering: A*, 395(1–2):110–115, 2005. doi: 10.1016/j.msea.2004.12.004.

R. A. Barrett, P. E. O'Donoghue, and S. B. Leen. An improved unified viscoplastic constitutive model for strain-rate sensitivity in high temperature fatigue. *International Journal of Fatigue*, 48:192–204, 2013. doi: 10.1016/j.ijfatigue.2012.11.001.

T. Belytschko, W. K. Liu, and B. Moran. *Nonlinear Finite Elements for Continua and Structures*. John Wiley & Sons, 2000.

A. Benaarbia, Y. Rae, and W. Sun. Unified viscoplasticity modelling and its application to fatigue-creep behaviour of gas turbine rotor. *International Journal of Mechanical Sciences*, 136:36–49, 2018. doi: 10.1016/j.ijmecsci.2017.12.008.

H. Berns and W. Theisen. *Eisenwerkstoffe - Stahl und Gusseisen*. Springer Berlin Heidelberg, 2008. doi: 10.1007/978-3-540-79957-3.

J. L. Chaboche. Constitutive equations for cyclic plasticity and cyclic viscoplasticity. *International Journal of Plasticity*, 5(3): 247–302, 1989. doi: 10.1016/0749-6419(89)90015-6.

J. L. Chaboche and G. Rousselier. On the Plastic and Viscoplastic Constitutive Equations: Part II: Application of Internal Variable Concepts to the 316 Stainless Steel. *Journal of Pressure Vessel Technology*, 105(2):159–164, 1983. doi: 10.1115/1.3264258.

H. Chilukuru, K. Durst, S. Wadekar, M. Schwienheer, A. Scholz, C. Berger, K. H. Mayer, and W. Blum. Coarsening of precipitates and degradation of creep resistance in tempered martensite steels. *Materials Science and Engineering: A*, 510-511:81–87, 2009. doi: 10.1016/j.msea.2008.04.088.

I. Cormeau. Numerical stability in quasi-static elasto/visco-plasticity. *International Journal for Numerical Methods in Engineering*, 9(1):109–127, 1975. doi: 10.1002/nme.1620090110.

J. Eisenträger. *A Framework for Modeling The Mechanical Behavior of Tempered Martensitic Steels at High Temperatures*. PhD thesis, Otto von Guericke University Magdeburg, 2018.

J. Eisenträger, K. Naumenko, H. Altenbach, and E. Gariboldi. Analysis of Temperature and Strain Rate Dependencies of Softening Regime for Tempered Martensitic Steel. *The Journal of Strain Analysis for Engineering Design*, 52:226–238, 2017. doi: 10.1177/0309324717699746.

J. Eisenträger, K. Naumenko, and H. Altenbach. Calibration of a Phase Mixture Model for Hardening and Softening Regimes in Tempered Martensitic Steel Over Wide Stress and Temperature Ranges. *The Journal of Strain Analysis for Engineering Design*, 53:156–177, 2018a. doi: 10.1177/0309324718755956.

J. Eisenträger, K. Naumenko, and H. Altenbach. Numerical implementation of a phase mixture model for rate-dependent inelasticity of tempered martensitic steels. *Acta Mechanica*, 229:3051–3068, 2018b. doi: 10.1007/s00707-018-2151-1.

B. Fournier, M. Sauzay, M. Mottot, H. Brillet, I. Monnet, and A. Pineau. Experimentally Based Modelling of Cyclically Induced Softening in a Martensitic Steel at High Temperature. In I. A. Shibli, S. R. Holdsworth, and G. Merckling, editors, *ECCC Creep Conference*, pages 649–661. DES tech publications, 2005.

B. Fournier, M. Sauzay, F. Barcelo, E. Rauch, A. Renault, T. Cozzika, L. Dupuy, and A. Pineau. Creep-Fatigue Interactions in a 9 Pct Cr-1 Pct Mo Martensitic Steel: Part II. Microstructural Evolutions. *Metallurgical and Materials Transactions A*, 40(2): 330–341, 2009a. doi: 10.1007/s11661-008-9687-y.

B. Fournier, M. Sauzay, A. Renault, F. Barcelo, and A. Pineau. Microstructural evolutions and cyclic softening of 9%Cr martensitic steels. *Journal of Nuclear Materials*, 386-388:71–74, 2009b. doi: 10.1016/j.jnucmat.2008.12.061.

B. Fournier, M. Salvi, F. Dalle, Y. de Carlan, C. Caës, M. Sauzay, and A. Pineau. Lifetime prediction of 9–12%Cr martensitic steels subjected to creep–fatigue at high temperature. *International Journal of Fatigue*, 32(6):971–978, 2010. doi: 10.1016/j.ijfatigue.2009.10.017.

B. Fournier, F. Dalle, M. Sauzay, J. Longour, M. Salvi, C. Caës, I. Tournié, P.-F. Giroux, and S.-H. Kim. Comparison of various 9–12%Cr steels under fatigue and creep-fatigue loadings at high temperature. *Materials Science and Engineering: A*, 528 (22-23):6934–6945, 2011a. doi: 10.1016/j.msea.2011.05.046.

B. Fournier, M. Sauzay, and A. Pineau. Micromechanical model of the high temperature cyclic behavior of 9–12%Cr martensitic steels. *International Journal of Plasticity*, 27(11):1803–1816, 2011b. doi: 10.1016/j.ijplas.2011.05.007.

S. R. Ghorpade and B. V. Limaye. *A Course in Multivariable Calculus and Analysis*. Springer New York, 2010. doi: 10.1007/978-1-4419-1621-1.

P. F. Giroux, F. Dalle, M. Sauzay, J. Malaplate, B. Fournier, and A. F. Gourgues-Lorenzon. Mechanical and microstructural stability of P92 steel under uniaxial tension at high temperature. *Materials Science and Engineering: A*, 527(16-17):3984–3993, 2010. doi: 10.1016/j.msea.2010.03.001.

G. Götz. *Langzeitentwicklung der Mikrostruktur neuer 9-12% Chromstähle für den Einsatz in Kraftwerken*. PhD thesis, Universität Erlangen-Nürnberg, Erlangen-Nürnberg, 2004.

S. Hartmann and P. Haupt. Stress computation and consistent tangent operator using non-linear kinematic hardening models. *International Journal for Numerical Methods in Engineering*, 36(22):3801–3814, 1993. doi: 10.1002/nme.1620362204.

S. Hartmann, G. Lührs, and P. Haupt. An efficient stress algorithm with applications in viscoplasticity and plasticity. *International Journal for Numerical Methods in Engineering*, 40(6):991–1013, 1997. doi: 10.1002/(SICI)1097-0207(19970330)40:6<991::AID-NME98ater3.0.CO;2-H.

C. Hu and H. Liu. Implicit and explicit integration schemes in the anisotropic bounding surface plasticity model for cyclic behaviours of saturated clay. *Computers and Geotechnics*, 55:27–41, 2014. doi: 10.1016/j.compgeo.2013.07.012.

M. Itskov. *Tensor Algebra and Tensor Analysis for Engineers: With Applications to Continuum Mechanics*. Springer International Publishing, 2019. doi: 10.1007/978-3-319-98806-1.

J. P. Jing, Y. Sun, S. B. Xia, and G. T. Feng. A continuum damage mechanics model on low cycle fatigue life assessment of steam turbine rotor. *International Journal of Pressure Vessels and Piping*, 78(1):59–64, 2001. doi: 10.1016/s0308-0161(01)00005-9.

J. P. Jing, G. Meng, Y. Sun, and S. B. Xia. An effective continuum damage mechanics model for creep-fatigue life assessment of a steam turbine rotor. *International Journal of Pressure Vessels and Piping*, 80(6):389–396, 2003. doi: 10.1016/s0308-0161(03)00070-x.

M. Kobayashi, M. Mukai, H. Takahashi, N. Ohno, T. Kawakami, and T. Ishikawa. Implicit integration and consistent tangent modulus of a time-dependent non-unified constitutive model. *International Journal for Numerical Methods in Engineering*, 58(10):1523–1543, 2003. doi: 10.1002/nme.825.

Y. Kostenko, H. Almstedt, K. Naumenko, S. Linn, and A. Scholz. Robust Methods for Creep Fatigue Analysis of Power Plant Components Under Cyclic Transient Thermal Loading. In *ASME Turbo Expo 2013: Turbine Technical Conference and Exposition*, volume Volume 5B: Oil and Gas Applications; Steam Turbines. Siemens Energy, Inc., 2013. doi: 10.1115/GT2013-95680.

L. X. Luccioni, J. M. Pestana, and R. L. Taylor. Finite element implementation of non-linear elastoplastic constitutive laws using local and global explicit algorithms with automatic error control. *International Journal for Numerical Methods in Engineering*, 50(5):1191–1212, 2001. doi: 10.1002/1097-0207(20010220)50:5<1191::AID-NME73>3.0.CO;2-T.

M. T. Manzari and R. Prachathananukit. On integration of a cyclic soil plasticity model. *International Journal for Numerical and Analytical Methods in Geomechanics*, 25(6):525–549, 2001. doi: 10.1002/nag.140.

K. Naumenko and H. Altenbach. *Modeling High Temperature Materials Behavior for Structural Analysis: Part I: Continuum Mechanics Foundations and Constitutive Models*. Advanced Structured Materials. Springer International Publishing, 2016. doi: 10.1007/978-3-319-31629-1.

K. Naumenko, H. Altenbach, and A. Kutschke. A Combined Model for Hardening, Softening, and Damage Processes in Advanced Heat Resistant Steels at Elevated Temperature. *International Journal of Damage Mechanics*, 20(4):578–597, 2011a. doi: 10.1177/1056789510386851.

K. Naumenko, A. Kutschke, Y. Kostenko, and T. Rudolf. Multi-axial thermo-mechanical analysis of power plant components from 9–12% Cr steels at high temperature. *Engineering Fracture Mechanics*, 78(8):1657–1668, 2011b. doi: 10.1016/j.engfracmech.2010.12.002.

A. Nayebi, H. Ranjbar, and H. Rokhgireh. Analysis of unified continuum damage mechanics model of gas turbine rotor steel: Life assessment. *Proceedings of the Institution of Mechanical Engineers, Part L: Journal of Materials: Design and Applications*, 227(3):216–225, 2012. doi: 10.1177/1464420712456513.

A. Orlová, J. Buršík, K. Kuchřoavá, and V. Sklenička. Microstructural development during high temperature creep of 9% Cr steel. *Materials Science and Engineering A*, 245:39–48, 1998. doi: 10.1016/S0921-5093(97)00708-9.

C. Pétry and G. Lindet. Modelling creep behaviour and failure of 9Cr–0.5Mo–1.8W–VNb steel. *International Journal of Pressure Vessels and Piping*, 86(8):486–494, 2009. doi: 10.1016/j.ijpvp.2009.03.006.

P. Polcik. *Modellierung des Verformungsverhaltens der warmfesten 9-12% Chromstähle im Temperaturbereich von 550-650°C*. PhD thesis, Friedrich-Alexander-Universität, Erlangen-Nürnberg, 1998.

S. V. Raj, I. S. Iskovitz, and A. D. Freed. Modeling the Role of Dislocation Substructure during Class M and Exponential Creep. In A. S. Krausz and K. Krausz, editors, *Unified Constitutive Laws of Plastic Deformation*, pages 343–439. Academic Press, Inc., 1996.

D. R. Röttger. *Untersuchungen zum Wechselverformungs- und Zeitstandverhalten der Stähle X20CrMoV121 und X10CrMoVNb91*. PhD thesis, Universität GH, Essen, 1997.

A. A. Saad. *Cyclic plasticity and creep of power plant materials*. PhD thesis, University of Nottingham, Nottingham, 2012. URL http://eprints.nottingham.ac.uk/id/eprint/12538.

A. V. Shutov and R. Kreißig. Finite strain viscoplasticity with nonlinear kinematic hardening: Phenomenological modeling and time integration. *Computer Methods in Applied Mechanics and Engineering*, 197(21-24):2015–2029, 2008. doi: 10.1016/j.cma.2007.12.017.

C. B. Silbermann, A. V. Shutov, and J. Ihlemann. Modeling the evolution of dislocation populations under non-proportional loading. *International Journal of Plasticity*, 55:58–79, 2014. doi: 10.1016/j.ijplas.2013.09.007.

J. C. Simo and T. J. R. Hughes. *Computational Inelasticity*. Springer, 1998. doi: 10.1007/b98904.

J. C. Simo and R. L. Taylor. Consistent tangent operators for rate-independent elastoplasticity. *Computer Methods in Applied Mechanics and Engineering*, 48(1):101–118, 1985. doi: 10.1016/0045-7825(85)90070-2.

S. Straub. *Verformungsverhalten und Mikrostruktur warmfester martensitischer 12%-Chromstähle*. PhD thesis, Friedrich-Alexander-Universität, Erlangen-Nürnberg, 1995.

Y.-J. Sun, X.-Q. Liu, L.-S. Hu, and X.-Y. Tang. Online life estimation for steam turbine rotor. *Journal of Loss Prevention in the Process Industries*, 26(1):272–279, 2013. doi: 10.1016/j.jlp.2012.11.008.

V. Velay, G. Bernhart, and L. Penazzi. Cyclic behavior modeling of a tempered martensitic hot work tool steel. *International Journal of Plasticity*, 22(3):459–496, 2006. doi: 10.1016/j.ijplas.2005.03.007.

J. Wang, P. Steinmann, J. Rudolph, and A. Willuweit. Simulation of creep and cyclic viscoplastic strains in high-Cr steel components based on a modified Becker–Hackenberg model. *International Journal of Pressure Vessels and Piping*, 128: 36–47, 2015. doi: 10.1016/j.ijpvp.2015.02.003.

L. Wang, M. Li, and J. Almer. In situ characterization of Grade 92 steel during tensile deformation using concurrent high energy X-ray diffraction and small angle X-ray scattering. *Journal of Nuclear Materials*, 440(1-3):81–90, 2013. doi: 10.1016/j.jnucmat.2013.04.063.

W. Z. Wang and Y. Z. Liu. Continuum damage mechanics-based analysis of creep-fatigue interaction behavior in a turbine rotor. *International Journal of Damage Mechanics*, 2018. doi: 10.1177/1056789518775174.

W. Z. Wang, P. Buhl, A. Klenk, and Y. Z. Liu. The effect of in-service steam temperature transients on the damage behavior of a steam turbine rotor. *International Journal of Fatigue*, 87:471–483, 2016. doi: 10.1016/j.ijfatigue.2016.02.040.

P. Wriggers. *Nonlinear Finite Element Methods*. Springer Berlin Heidelberg, 2008. doi: 10.1007/978-3-540-71001-1.

S.-L. Zhang and F.-Z. Xuan. Interaction of cyclic softening and stress relaxation of 9–12% Cr steel under strain-controlled fatigue-creep condition: Experimental and modeling. *International Journal of Plasticity*, 98:45–64, 2017. doi: 10.1016/j.ijplas.2017.06.007.

X. Zhu, H. Chen, F. Xuan, and X. Chen. Cyclic plasticity behaviors of steam turbine rotor subjected to cyclic thermal and mechanical loads. *European Journal of Mechanics A/Solids*, 66:243–255, 2017. doi: 10.1016/j.euromechsol.2017.07.012.

Y. Zhu, G. Kang, Q. Kan, and O. T. Bruhns. Logarithmic stress rate based constitutive model for cyclic loading in finite plasticity. *International Journal of Plasticity*, 54:34–55, 2014. doi: 10.1016/j.ijplas.2013.08.004.

O. C. Zienkiewicz and R. L. Taylor. *The finite element method for solid and structural mechanics*. Elsevier Butterworth-Heinemann, Amsterdam and Boston, 2005.